Presynaptic inhibition selectively suppresses leg proprioception in behaving *Drosophila*

Chris J. Dallmann [1,3], Sweta Agrawal [1,4], Andrew Cook [1], Bingni W. Brunton [2], and John C. Tuthill [1,5]

[1]Department of Physiology and Biophysics, University of Washington, Seattle, WA, USA; [2]Department of Biology, University of Washington, Seattle, WA, USA; [3]Present address: Department of Neurobiology and Genetics, Julius-Maximilians-University of Würzburg, Würzburg, Germany; [4]Present address: School of Neuroscience, Virginia Tech, Blacksburg, VA, USA; [5]Lead contact

The sense of proprioception is mediated by internal mechanosensory neurons that detect joint position and movement. To support a diverse range of functions, from stabilizing posture to coordinating movements, proprioceptive feedback to limb motor control circuits must be tuned in a context-dependent manner. How proprioceptive feedback signals are tuned to match behavioral demands remains poorly understood. Using calcium imaging in behaving *Drosophila*, we find that the axons of position-encoding leg proprioceptors are active across behaviors, whereas the axons of movement-encoding leg proprioceptors are suppressed during walking and grooming. Using connectomics, we identify a specific class of interneurons that provide GABAergic presynaptic inhibition to the axons of movement-encoding proprioceptors. These interneurons are active during self-generated but not passive leg movements and receive input from descending neurons, suggesting they are driven by predictions of leg movement originating in the brain. Predictively suppressing expected proprioceptive feedback provides a mechanism to attenuate reflexes that would otherwise interfere with voluntary movement.

Motor control, proprioception, presynaptic inhibition, predictive signaling, efference copy, corollary discharge, ventral nerve cord, *Drosophila*

Correspondence: ***tuthill@uw.edu***

Introduction

Effective motor control of the arms and legs requires sensory feedback from proprioceptive sensory neurons (i.e., proprioceptors) that detect the position and movement of the body (Proske and Gandevia 2012; Tuthill and Azim 2018). Motor circuits in the central nervous system integrate proprioceptive information at multiple levels to refine motor output and support a range of motor functions, from postural stabilization to adaptive locomotion (Rossignol et al. 2006; Dallmann et al. 2021; Frigon et al. 2021).

Because the same proprioceptors are used for many different motor control tasks, proprioceptive feedback must be flexibly tuned depending on the behavioral context (Azim and Seki 2019). For example, inhibition of proprioceptive pathways during voluntary movement can suppress stabilizing reflexes that would oppose the intended movement (McComas 2016). Context-dependent tuning of proprioceptive feedback may also prevent instabilities due to inherent delays in sensory pathways (Fink et al. 2014). This is seen in mice, where proprioceptive feedback is inhibited during walking and reaching to ensure smooth movement execution (Fink et al. 2014; Koch et al. 2017).

An efficient means of flexibly tuning sensory feedback pathways is predictive inhibition. In theoretical frameworks of predictive inhibition, the motor circuits send an inhibitory signal to the sensory circuits that is based on the motor commands (Figure 1A; Crapse and Sommer 2008; Straka et al. 2018). This mechanism, called efference copy or corollary discharge, allows self-generated sensory signals to be attenuated or completely canceled out, while externally-generated sensory signals are still transmitted to motor circuits. In the case of proprioceptive feedback, this ensures that stabilizing reflexes are recruited only in response to external forces (perturbations), not voluntary movement.

Predictive inhibition of sensory feedback has been described for many different sensory modalities across multiple species (Cullen 2004; Crapse and Sommer 2008; Straka et al. 2018; Azim and Seki 2019; Daly and Dacks 2023). Inhibition can occur at multiple levels of the nervous system, but a common mechanism is presynaptic inhibition, where inhibitory neurons directly target the sensory axon terminals to reduce neurotransmitter release (Clarac and Cattaert 1996; Rudomin and Schmidt 1999). Previous studies have shown that presynaptic inhibition can dynamically suppress sensory transmission in proprioceptive axons, consistent with the theoretical framework of predictive inhibition. For example, the axons of leg proprioceptors in mice (Koch et al. 2017) and locusts (Wolf and Burrows 1995) receive GABAergic inhibition during walking. However, the extent to which specific proprioceptive feedback pathways are inhibited during behavior and the central circuits that mediate the inhibition have remained challenging to study. This is due in part to the complexity of the underlying circuits and the technical difficulty of recording from identified neurons in the spinal cord and ventral nerve cord (VNC) in behaving animals.

Here, we investigate presynaptic inhibition of leg proprioception in the fruit fly, *Drosophila melanogaster*. We focus on the femoral chordotonal organ (FeCO), the

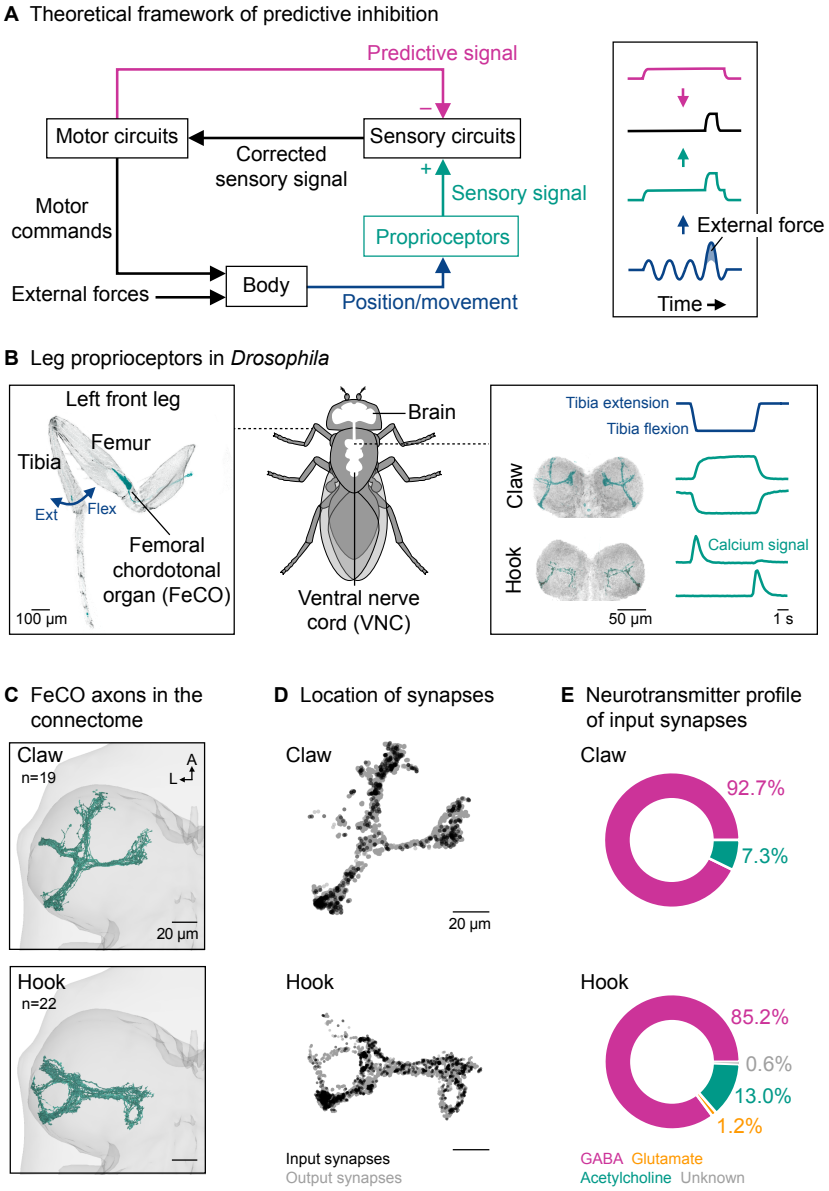

Figure 1. Proprioceptor axons from the *Drosophila* leg are anatomically positioned to receive presynaptic inhibition

(A) Left: A theoretical framework for predictive inhibition of proprioceptive pathways. High- or low-level motor circuits send a predictive inhibitory signal based on the motor commands to the sensory circuits. The predictive signal is subtracted from the measured sensory signal. The corrected sensory signal can be used to counteract external forces without impeding voluntary movement. Right: Schematic time courses of a joint angle (blue) resulting from self-generated motor commands and external forces, the sensory signal (green) representing both components, and the corrected sensory signal (black) after subtraction of the predictive signal (magenta). The example illustrates a case where the predictive signal matches the sensory signal in timing and amplitude.

(B) Left: Confocal image of a *Drosophila* front leg showing the location of the femoral chordotonal organ (FeCO) cell bodies and dendrites. Green: GFP; gray: cuticle auto-fluorescence. The blue arrow indicates the extension (Ext) and flexion (Flex) of the tibia relative to the femur. Right: Confocal image of position-encoding claw and movement-encoding hook axons in the fly ventral nerve cord (VNC). Flexion- and extension-encoding hook axons are overlayed. Green: GFP; gray: neuropil stain (nc82). Schematized calcium signals from claw and hook axons (GCaMP, green) in response to a controlled, passive movement of the femur-tibia joint (blue) based on Mamiya et al. (2023).

(C) Top view of reconstructed claw and hook axons in the left front leg neuromere of the FANC connectome. n: number of axons; A: anterior; L: lateral.

(D) Location of input and output synapses of all reconstructed claw and hook axons. View as in (C).

(E) Neurotransmitter profile of the input synapses of claw and hook axons.

See also Figure S1 and Video S1.

largest proprioceptive organ in the fly leg (Figure 1B, left; Kuan et al. 2020). The FeCO is functionally analogous to vertebrate muscle spindles (Tuthill and Azim 2018). Genetically distinct "claw" and "hook" FeCO neurons monitor the position and movement of the tibia, respectively (Mamiya et al. 2018, 2023). Position-encoding claw neurons are tonically active at different joint angles, whereas movement-encoding hook neurons are phasic and directionally tuned (Figure 1B, right). Feedback from FeCO neurons is integrated by circuits in the VNC to control leg posture and movement (Agrawal et al. 2020; Chen et al. 2021; Chockley et al. 2022). However, the activity of FeCO neurons in *Drosophila* has only been studied during passive leg movements, delivered with a magnetic control system (Mamiya et al. 2018, 2023). Thus, it remains an open question whether FeCO neurons receive presynaptic inhibition during active, self-generated leg movements.

To address this question, we reconstructed FeCO axons in a VNC connectome and found that they receive significant presynaptic input from GABAergic interneurons. To determine whether FeCO axons are suppressed during behavior, we used calcium imaging to record proprioceptor activity in tethered flies behaving on a treadmill. While the axons of position-encoding claw neurons were active across behaviors, the axons of movement-encoding hook neurons were suppressed during walking and grooming. Using the connectome, we identified a specific class of GABAergic interneurons that provides the majority of presynaptic input to hook axons. Calcium imaging from these interneurons revealed that they are active during self-generated but not passive leg movements, consistent with their role in inhibiting proprioceptor axons during voluntary movement. These GABAergic neurons receive input from descending neurons suggesting they are driven by predictions of leg movement originating in the brain. Overall, our findings establish a neural circuit for selectively suppressing the output of movement-encoding proprioceptors during self-generated limb movements.

Results

Proprioceptor axons from the *Drosophila* leg are anatomically positioned to receive presynaptic inhibition

To determine whether proprioceptor axons receive presynaptic input, we first reconstructed FeCO axons in an electron microscopy volume of a female *Drosophila* VNC (FANC; Phelps et al. 2021). We took advantage of automated tools for neuron segmentation and synapse prediction (Azevedo et al. 2022), and then manually proofread each axon for accuracy. We reconstructed 19 of ~30 claw axons and 22 of ~56 hook axons in the neuromere of the left front leg (Figure 1C and S1; Video S1).

We then analyzed the location and number of the input and output synapses of the FeCO axons (Figure 1D). Input synapses were present on all axon branches, spatially intermingled with output synapses. On average, individual claw and hook axons had 29$\pm$18 (mean$\pm$std) and 63$\pm$41 input synapses and 744$\pm$311 and 787$\pm$380 output synapses, respectively. Individual axons differed in the total number of synapses; the number of input synapses was weakly correlated with the number of output synapses (claw: R^2=0.62; hook: R^2=0.20; Figure S1C). By identifying the neurons presynaptic to claw and hook axons (see methods), we found that the presynaptic partners were primarily GABAergic (Figure 1E). Consistent with this finding, we analyzed a single-cell RNA-sequencing dataset (Mamiya et al. 2023) and found that all claw and hook neurons strongly express Rdl, the gene for $GABA_A$ receptors. In contrast, the gene for the inhibitory glutamate receptor GluClα was only weakly expressed in a few FeCO cells.

Together, connectomic reconstruction and RNA-sequencing data of claw and hook neurons suggest that they receive GABAergic input from VNC interneurons, which provides a substrate for context-dependent presynaptic inhibition.

Tools to study leg proprioception in behaving *Drosophila*

To investigate the function of presynaptic inhibition of FeCO axons, we developed a setup for two-photon calcium imaging of neural activity in the VNC and 3D leg tracking of tethered flies on a spherical treadmill (Figure 2A; see methods). The setup allowed us to record calcium signals in FeCO axons and other VNC neurons with GCaMP while flies walked, groomed, or rested on the treadmill.

To identify context-dependent inhibition of FeCO axons, we sought to compare proprioceptor activity during active (i.e., self-generated) and passive (i.e., externally-imposed) leg movements. Because it was not technically feasible to do this comparison directly within the same animal, we constructed computational models that replicated calcium signals in FeCO axons during passive leg movements (Figure 2B). The models convolved a claw- or hook-specific activation function with a GCaMP kernel to translate time courses of femur-tibia kinematics into time courses of calcium signals. We then used these models to predict calcium signals in FeCO axons during active leg movements (Figure 2D). This comparison of predicted calcium signals based on passive leg movements and measured calcium signals during active leg movements provides a quantitative means to identify context-dependent inhibition.

The activation functions within each model were based on our previous calcium imaging and leg tracking data, in which the femur-tibia joint was passively moved (Mamiya et al. 2018; see methods; Figure S2A). As a population, claw neurons encode the position of the femur-tibia joint as a deviation from a joint angle of ~80°. Population activity increases non-linearly with increasing flexion or extension (Figure S2B). In contrast,

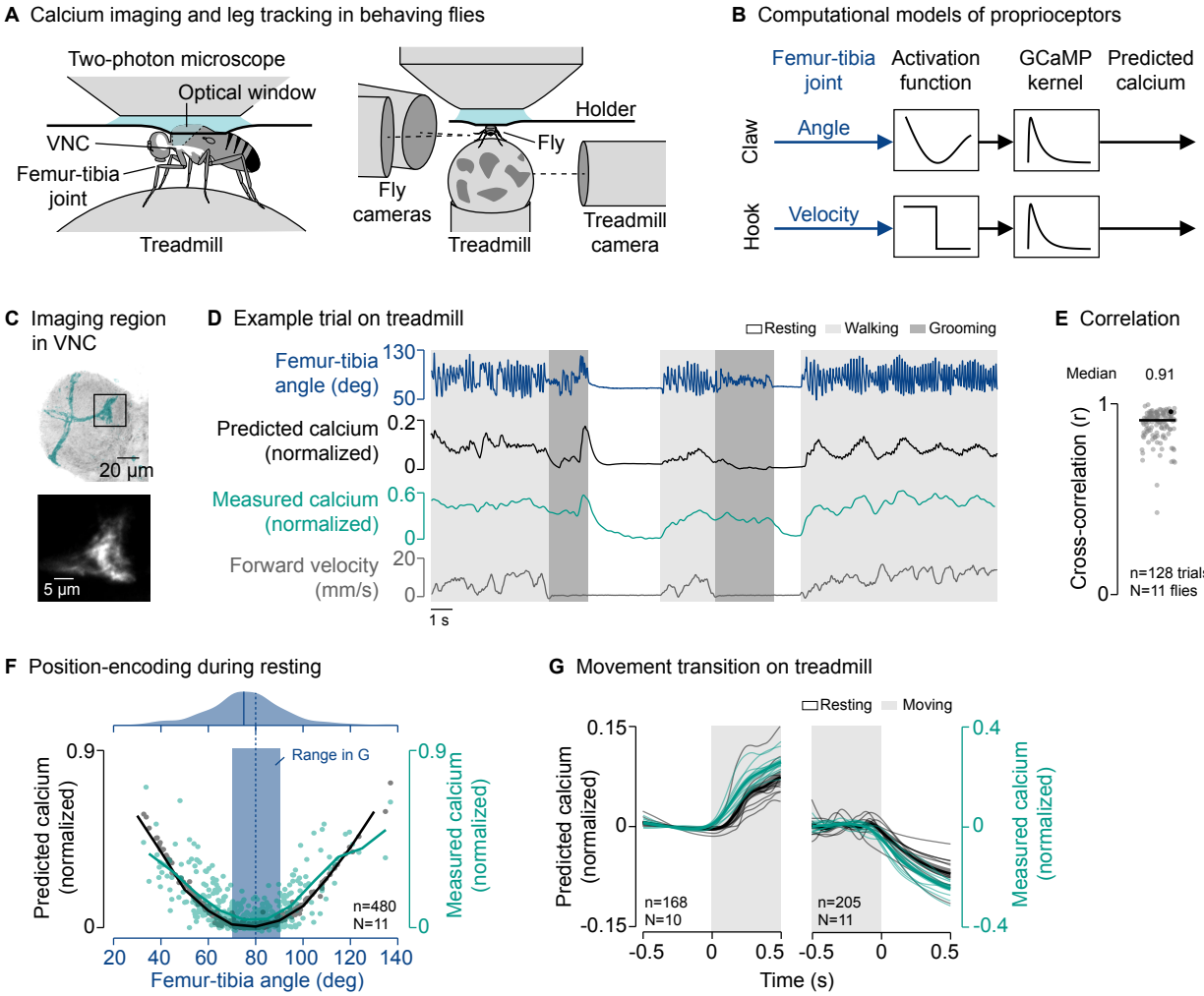

Figure 2. The axons of position-encoding (claw) proprioceptors are not suppressed during active leg movements

(A) Experimental setup for two-photon calcium imaging from VNC neurons and 3D leg tracking of the left front leg of tethered flies on a treadmill.

(B) Computational models of FeCO proprioceptors translating time courses of joint angles into time courses of calcium signals. The activation functions were fitted to calcium signals measured during passive leg movement.

(C) Top: Confocal image of position-encoding claw axons in the VNC. The black box indicates the imaging region. Green: GFP; gray: neuropil stain (nc82). A: anterior; L: lateral. Bottom: Mean tdTomato signal within the imaging region during an example trial.

(D) Example trial of two-photon calcium imaging of claw axons and behavior tracking on the treadmill.

(E) Cross-correlation coefficient between predicted and measured calcium signals per trial at a time lag of zero. The black line shows the median. The black dot marks the trial shown in (D). n: number of trials; N: number of flies.

(F) Median predicted and measured calcium signals as a function of the median femur-tibia angle for individual resting bouts. Bouts are $\geq$1 s in duration. The black and green line indicate the mean calcium signals in bins of 10°. The dashed blue line indicates the resting angle at which activity is minimal. The blue rectangle indicates the range of resting angles analyzed in (G). The plot on top shows a kernel density estimation of the femur-tibia angles during resting. The solid blue line indicates the most frequent femur-tibia angle (mode of the distribution). n: number of resting bouts; N: number of flies.

(G) Predicted and measured calcium signals aligned to the transitions into and out of movement. Movement includes walking and grooming. Thin lines show animal means, thick lines show mean of means, shadings show standard error of the mean. n: number of transitions; N: number of flies.

See also Figure S2 and Video S2.

hook neurons respond transiently to flexion or extension of the femur-tibia joint (Figure S2D). Our claw and hook models effectively replicated these characteristic calcium signals during passive leg movements (Figure S2B and S2D). This was reflected in high cross-correlation coefficients between measured and predicted calcium signals across trials and flies (claw: r=0.93; hook: r=0.84; Figure S2C and S2E).

Together, the experimental setup and computational models enabled us to record calcium signals in proprioceptor axons and identify differences in activity between self-generated and passive leg movements.

The axons of position-encoding proprioceptors are not suppressed during active leg movements

Equipped with computational models to predict calcium signals during active leg movements, we first asked whether the axons of the position-encoding claw neurons are suppressed during behavior. We co-expressed the calcium indicator GCaMP and the structural marker tdTomato with the same genetic driver line that was used to tune the passive computational model (Figure 2C), and recorded the activity of claw axons in behaving flies.

Claw axons were active across behaviors—during

resting, walking, and grooming (Figure 2D; Video S2). The passive model effectively tracked the temporal dynamics of the calcium signal across different behaviors (Figure 2D). This was reflected in high cross-correlation coefficients between measured and predicted calcium signals across trials and flies (r=0.91; Figure 2E), which were comparable to those in the passive movement experiments used to tune the passive model (Figure S2C). Calcium signals were also well predicted when we removed the treadmill and flies moved their legs freely in the air (Figure S2F and S2G; Video S2).

The characteristic position-encoding of claw axons was particularly clear when resting flies held their front leg at a given femur-tibia angle for an extended period of time. Plotting the median amplitude of the calcium signal against the median femur-tibia joint angle for individual resting bouts ($\geq$1 s in duration) revealed the expected U-shaped activity pattern centered at ~80° (Figure 2F, bottom). The minimum signal was close to the most frequent femur-tibia angle that flies adopted while resting on the treadmill (75°; Figure 2F, top).

Given this U-shaped activity pattern, we expected to see strong changes in the calcium signal when flies transitioned between resting and moving near the most frequent resting angle. Indeed, for transitions toward or away from resting angles of 70°-90° (Figure 2F, blue box), calcium signals increased and decreased as predicted by the passive model (Figure 2G).

Together, these results indicate that the position-encoding claw axons are not suppressed during self-generated leg movements. Rather, the results indicate that position feedback is transmitted to downstream VNC neurons across behavioral contexts. The close match between the passive claw model predictions and calcium signals recorded during behavior also provides confidence in our approach of comparing self-generated and passive leg movements in leg proprioceptors.

The axons of movement-encoding proprioceptors are suppressed during active leg movements

We next asked whether the axons of movement-encoding proprioceptors are suppressed during behavior. We first investigated hook neurons encoding tibia flexion movements. We again co-expressed the calcium indicator GCaMP and the structural marker tdTomato in the same driver line used for tuning the passive computational model (Figure 3A), and recorded the activity of hook axons in behaving flies.

The passive model predicted strong calcium signals in hook axons during walking and grooming compared to resting (Figure 3B and 3D). However, hook calcium signals recorded during behavior were conspicuously different from the passive model predictions (Figure 3B and 3D; Video S3). The discrepancy between model prediction and measurement was particularly clear at the transitions into and out of movement, at which calcium signals did not increase or decrease as predicted by the passive model (Figure 3E). Accordingly, the cross-correlation between measured and predicted calcium signals across trials and flies was more variable and lower on average than during passive movement (r=0.68; Figure 3C, Treadmill). Note that we computed high cross-correlation coefficients in some trials simply because the fly's behavior, and with that, the predicted calcium signals, changed little over time. Calcium signals were also absent when we removed the treadmill and flies moved their legs freely in the air (Figure S3A–C; Video S3). The lack of calcium signals during self-generated movements was even more pronounced in a second driver line for hook flexion neurons (Figure S3D–I). We observed a similar degree of behavioral state-dependent suppression in hook neurons encoding tibia extension movements (Figure S4). These results indicate that both extension- and flexion-encoding hook axons are suppressed during self-generated but not passive leg movements.

Supporting this conclusion, we observed that calcium signals were high when the front leg was moved passively while resting on the treadmill, which sometimes occurred when the hind legs lifted off the treadmill for grooming (Video S3). Calcium signals were also high during resting when the front leg slowly (over the course of hundreds of milliseconds) moved towards flexion, which we observed after front leg grooming when the leg was not placed on the treadmill (Figure 3B, asterisks) or in trials in which the treadmill was removed (Figure S3A). These slow flexions were likely the result of passive forces produced by leg muscles and skeletal structures (Hooper et al. 2009; Ache and Matheson 2013).

To further test that hook axons are not suppressed during passive movements, we replaced the treadmill with a moveable platform that flies gripped with the tips of their legs (Figure 3F; Video S3). We used the platform to passively move the front leg while imaging from hook axons in the VNC. In this context, we measured strong calcium signals in response to passive movement of the femur-tibia joint, as predicted by the passive model (Figure 3G and 3H). This was reflected in higher and less variable cross-correlation coefficients between predicted and measured calcium signals across trials and flies (r=0.86; Figure 3C, Platform).

Finally, we asked whether differences between the passive model predictions and recorded calcium signals could be due to differences in joint movement dynamics between the active and passive movement conditions. Specifically, flies tended to move their legs more rapidly when they were actively moving compared to how we moved them during passive stimulation with the platform. Using the same magnetic control system in which we previously investigated proprioceptor responses to passive movements (Mamiya et al. 2018, 2023), we replayed naturalistic time courses of femur-tibia joint angles measured during walking and grooming to otherwise passive animals (Figure S5A and S5B; see methods). Calcium signals recorded from hook axons in this

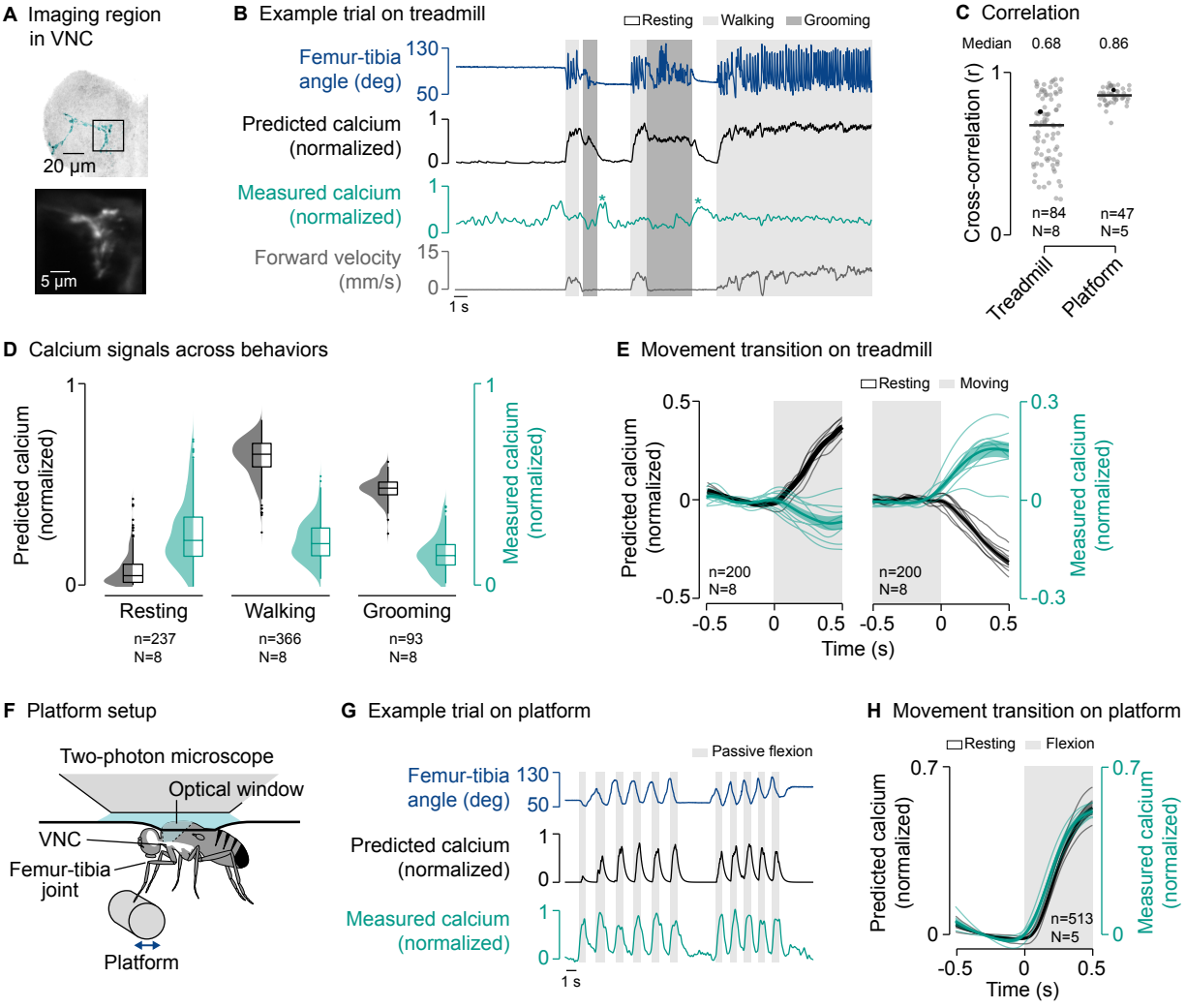

Figure 3. The axons of movement-encoding (hook) proprioceptors are suppressed during active leg movements

(A) Top: Confocal image of movement-encoding hook axons in the VNC. The black box indicates the imaging region. Green: GFP; gray: neuropil stain (nc82). A: anterior; L: lateral. Bottom: Mean tdTomato signal within the imaging region during an example trial.

(B) Example trial of two-photon calcium imaging of hook flexion axons and behavior tracking on the treadmill. The asterisks highlight resting bouts during which the front leg was held in the air and slowly flexed, likely as a result of passive forces produced by leg muscles and skeletal structures.

(C) Cross-correlation coefficient between predicted and measured calcium signals per trial at a time lag of zero in different movement contexts. Black lines show medians. Black dots mark the trials shown in (B) and (G). n: number of trials; N: number of flies.

(D) Median predicted and measured calcium signals during resting, walking, and grooming. Bouts are $\geq$1 s in duration. Distributions show kernel density estimations. n: number of behavioral bouts; N: number of flies.

(E) Predicted and measured calcium signals aligned to the transitions into and out of movement. Signals are baseline subtracted (mean from -0.5 to 0 s). Movement includes walking and grooming. Thin lines show animal means, thick lines show mean of means, shadings show standard error of the mean. n: number of transitions; N: number of flies.

(F) Experimental setup for passively moving the left front leg via a platform during two-photon calcium imaging from the VNC.

(G) Example trial of two-photon calcium imaging of hook flexion axons and behavior tracking on the platform.

(H) Predicted and measured calcium signals aligned to the transition into passive flexion of the femur-tibia joint. Lines and labels as in (E).

See also Figures S3–S5 and Video S3.

passive context matched the predictions of the passive model (Figure S5C and S5E), with calcium signals increasing at the onset of movement as predicted (Figure S5D and S5F). Thus, the discrepancy between activity recorded during self-generated movements and the passive model predictions is unlikely to be caused by differences in stimulus statistics.

Together, these results indicate that movement-encoding hook axons are suppressed whenever flies move their legs actively, regardless of the specific movement context.

GABAergic interneurons provide presynaptic inhibition to movement-encoding proprioceptor axons

To explore the circuit mechanisms underlying the selective suppression of hook axons, we analyzed the presynaptic connectivity of claw and hook axons in the VNC connectome (Figure 4A). Claw and hook axons receive input from interneurons and sensory neurons local to the VNC, but not descending neurons (claw: 100% interneurons; hook: 94.9% interneurons, 4.6% sensory neurons, 0.5% unidentified). On average, hook axons receive more presynaptic input than claw axons (Figure

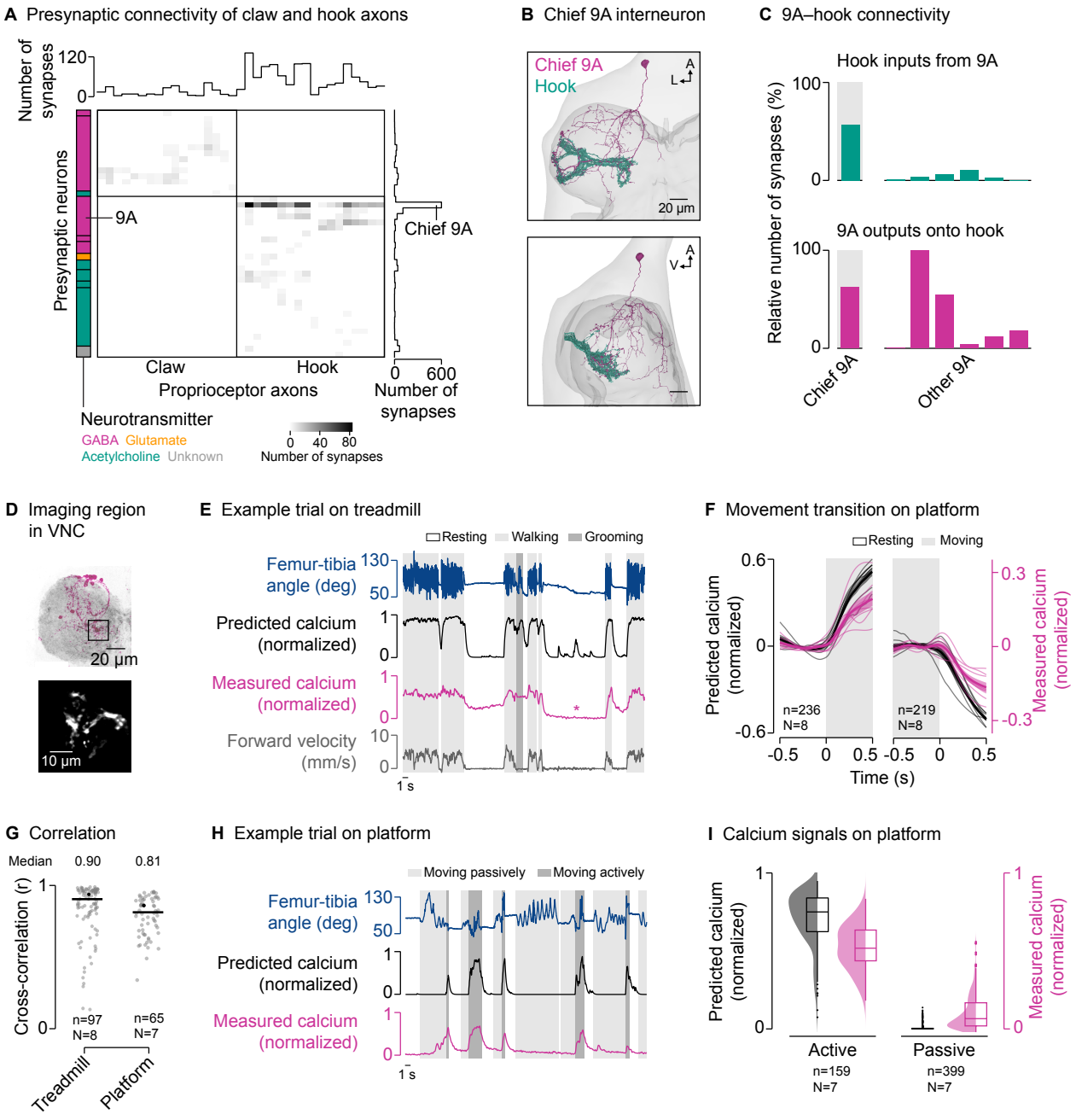

Figure 4. GABAergic interneurons provide presynaptic inhibition to movement-encoding proprioceptor axons

(A) Connectivity of presynaptic neurons with claw and hook axons. The grayscale heatmap indicates the number of synapses between neurons (connection strength). Boxes on the left group presynaptic neurons of the same developmental lineage, with the color indicating their primary fast-acting neurotransmitter. Boxes from top to bottom: 13B and 19A (both GABA); 3A (acetylcholine); 9A, 13B, and 19A (all GABA); 8A (glutamate); 8B, 18B, 22A, and sensory (all acetylcholine); unknown.

(B) Top and side view of the chief GABAergic 9A interneuron presynaptic to hook axons in the left front leg neuromere in FANC. A: anterior; L: lateral; V: ventral.

(C) Connectivity between 9A neurons and hook axons.

(D) Top: Confocal image of 9A neurons in the VNC. The black box indicates the imaging region. Magenta: GFP; gray: neuropil stain (nc82). A: anterior; L: lateral. Bottom: Mean tdTomato signal within the imaging region during an example trial.

(E) Example trial of two-photon calcium imaging of 9A neurons and behavior tracking on the treadmill. The asterisk highlights a resting bout during which the front leg was moved passively by hind leg grooming.

(F) Predicted and measured calcium signals aligned to the transitions into and out of movement. Movement includes walking and grooming. Thin lines show animal means, thick lines show mean of means, shadings show standard error of the mean. n: number of transitions; N: number of flies.

(G) Cross-correlation coefficient between predicted and measured calcium signals per trial at a time lag of zero in different movement contexts. Black lines show medians. Black dots mark the trials shown in (E) and (H). n: number of trials; N: number of flies.

(H) Example trial of two-photon calcium imaging of 9A neurons and behavior tracking on the platform.

(I) Median predicted and measured calcium signals during active and passive movement bouts on the platform. Bouts are $\geq$1 s in duration. Distributions show kernel density estimations. n: number of movement bouts; N: number of flies.

See also Figure S6 and Video S4.

4A, top), with most input coming from GABAergic interneurons. Interestingly, presynaptic neurons target either claw axons or hook axons, but not both. This could help explain why activity was selectively suppressed in hook axons but not claw axons. Most GABAergic input onto hook axons (83.1%) comes from a group of local interneurons belonging to the 9A hemilineage (Harris et al. 2015). One 9A neuron in particular provides 56.8% of presynaptic input to hook axons (Figure 4A, right). This chief 9A neuron receives dendritic input in the dorsal VNC and provides synaptic output to hook axons in the the ventral VNC (Figure 4B). In fact, most of the output of the chief 9A neuron (62.8%) is onto hook axons (Figure 4C). Other GABAergic neurons of the 9A hemilineage also provide a significant fraction of their output to hook axons (Figure 4C). Thus, this group of GABAergic 9A interneurons is positioned to selectively suppress activity in hook axons during active leg movements via presynaptic inhibition.

If these 9A interneurons suppress activity in hook axons, we would expect their activity to be high during active leg movements and low during passive leg movements; the opposite activity pattern that we observed in hook axons. We instantiated this prediction in a simple computational model, in which calcium activity is high during active flexion and extension movements, but not during resting or passive leg movements (Figure S2A; see methods). We then compared the predictions of the model to calcium imaging data from 9A interneurons, focusing on a region near the terminals of hook axons (Figure 4D). As predicted, we measured strong calcium signals in the axons of the 9A interneurons during walking and grooming (Figure 4E; Video S4), with calcium signals increasing and decreasing at the transitions into and out of movement, respectively (Figure 4F). This was reflected in high cross-correlation coefficients between predicted and measured calcium signals across trials and flies (r=0.90; Figure 4G). Calcium signals were also well predicted when we removed the treadmill and flies moved their legs freely in the air (r=0.95; Figure S6; Video S4).

Calcium signals in 9A axons were weak or absent when the front leg was moved passively on the treadmill, which sometimes occurred when the hind legs lifted off the treadmill for grooming (Figure 4E, asterisk; Video S4). To further test whether calcium signals in 9A axons are absent during passive leg movements, we again used the platform setup to passively move the femur-tibia joint (Figure 4H; Video S4). Because flies were not anesthetized, they sometimes actively moved their legs instead of gripping the platform. As predicted by the passive model, calcium signals were weak during passive leg movements and strong during active leg movements (Figure 4H and 4I), with high cross-correlation coefficients between predicted and measured calcium signals (r=0.81; Figure 4G).

These results demonstrate that local GABAergic 9A interneurons are active during self-generated but not passive leg movements. The synaptic connectivity and activity pattern of these neurons suggest that they selectively suppress hook axons via presynaptic inhibition. Notably, previous studies found that other neurons of the 9A hemilineage are postsynaptic to FeCO neurons (Agrawal et al. 2020) and presynaptic to motor neurons (Lesser et al. 2023). This suggests that although all 9A neurons are developmentally related, individual 9A neurons can have distinct circuit functions.

GABAergic interneurons receive descending input from the brain

To explore the origins of state-dependent activity in GABAergic 9A interneurons, we analyzed their presynaptic neurons in the connectome (Figure 5A). The 9A neurons receive little direct input from sensory neurons, suggesting they are not driven by sensory feedback from the leg. Interestingly, the chief 9A neuron, which provides the majority of the input to hook axons, receives most of its input (68%) from descending neurons. The other 9A neurons receive most of their input from local premotor neurons in the VNC, but some neurons of the group also receive descending input (Figure 5B). In fact, several specific descending neurons provide input to multiple 9A neurons (Figure 5B). Thus, the 9A neurons may be recruited together by descending input from the brain to presynaptically inhibit hook axons during behavior.

Some of the descending neurons presynaptic to the chief 9A interneuron target only the neuromere of the left front leg (Figure 5C), suggesting that the suppression of hook axons can be controlled in a leg-specific manner. However, the majority of descending input (78%) comes from intersegmental descending neurons that target multiple leg neuromeres of one body side (Figure 5C). This raised the possibility that the circuit motif we identified for the left front leg is present in all legs. To test this possibility, we turned to a second VNC connectome of a male fly, which is more fully reconstructed in the middle and rear neuromeres (MANC; see methods; Takemura et al. 2023; Marin et al. 2023). In support of our hypothesis, hook axons in all leg neuromeres receive most of their input from a GABAergic interneuron of the 9A hemilineage, which resembles the chief 9A interneuron reconstructed in the female connectome (Figure S7). Moreover, the top two presynaptic partners of these interneurons in the male connectome were intersegmental descending neurons whose morphology and connectivity matched the top two intersegmental descending neurons we identified in the female connectome (FANC; Figure S7). Thus, the inhibitory circuit motif is segmentally repeated to inhibit hook axons from all legs along each side of the body. While most of the descending neurons presynaptic to the 9A interneurons have not yet been identified in the connectome, some of them are known to drive walking (BDN2 and oDN1; Sapkal et al. 2023) and turning (DNa02 and DNg13; Yang et al. 2023), supporting our

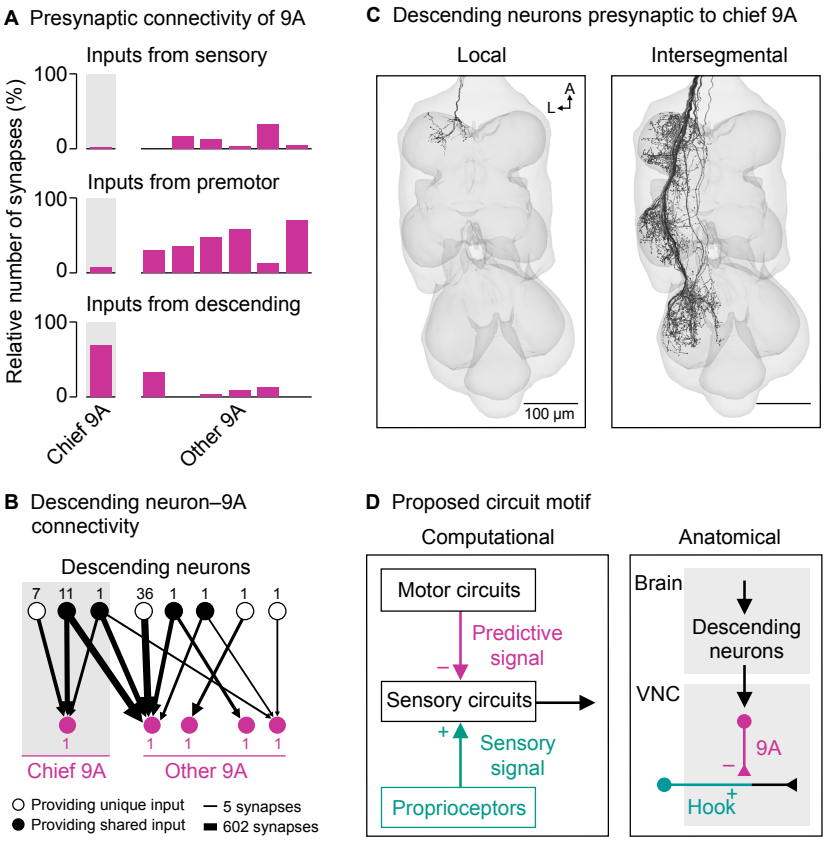

Figure 5. GABAergic interneurons receive descending input from the brain
(A) Inputs from sensory neurons, premotor neurons, and descending neurons onto individual 9A neurons presynaptic to hook axons.
(B) Connectivity between descending neurons and the 9A neurons presynaptic to hook axons that receive descending input. Numbers next to nodes indicate number of neurons.
(C) Local and intersegmental descending neurons presynaptic to the chief 9A neuron in FANC. A: anterior; L: lateral.
(D) Proposed circuit motif. A set of descending neurons carries information from the brain and targets 9A neurons in each leg neuromere to suppress hook feedback resulting from self-generated movement. The difference signal between predicted and measured feedback is transmitted to downstream VNC circuits.
See also Figure S7.

model that presynaptic inhibition of hook axons is driven by high-level motor circuits in the brain (Figure 5D).

Together, the presynaptic connectivity of the GABAergic 9A interneurons suggests that the suppression of hook axons during active leg movements is driven primarily by descending signals from the brain. The inhibitory circuit motif is consistent across two VNC connectomes and present in all leg neuromeres. This architecture suggests that proprioceptive feedback from movement-encoding proprioceptors is predictively suppressed across all legs during behavior.

Discussion

In this study, we elucidate a neural circuit that selectively suppresses proprioceptive feedback from the *Drosophila* leg in a behavioral state-dependent manner. Both position- and movement-encoding FeCO axons receive presynaptic input from GABAergic interneurons (Figure 1), but only the movement-encoding hook axons are suppressed during active movement (Figures 2 and 3). Hook axons receive presynaptic inhibition from a specific class of GABAergic interneurons (Figure 4). These neurons are active during self-generated but not passive leg movements (Figure 4) and receive input from descending neurons (Figure 5), suggesting they are driven by predictions of leg movement originating in the brain.

GABA-mediated suppression of hook axons

Our evidence suggests that hook axons are inhibited by GABA acting on $GABA_A$ receptors. Connectomics analysis revealed overwhelmingly GABAergic input onto hook axons, and our analysis of an RNA-sequencing dataset (Mamiya et al. 2023) revealed that hook neurons strongly express the $GABA_A$ receptor gene Rdl. GABAergic presynaptic inhibition of somatosensory axons is common throughout the animal kingdom (Rudomin and Schmidt 1999). For example, the axons of leg proprioceptors of locusts (Wolf and Burrows 1995) and mice (Koch et al. 2017) receive GABAergic presynaptic inhibition during walking. Notably, presynaptic inhibition can also be mediated by other neurotransmitters, including glutamate (Lin et al. 2023; Rudomin and Schmidt 1999). In the case of hook axons, however, the low number of glutamatergic input synapses in the connectome and the low expression level of the inhibitory glutamate receptor gene

GluClα argue against glutamatergic inhibition as the driving force.

Behavioral function of sensory suppression in hook axons

How might presynaptic inhibition of hook axons affect leg motor control? Studies in a range of insects have shown that FeCO neurons mediate stabilizing reflexes of the tibia in response to external perturbations (Bässler 1993; Field and Matheson 1998; Tuthill and Wilson 2016). In *Drosophila*, a passive extension of the tibia excites motor neurons innervating the muscles that flex the tibia, leading to a compensatory flexion of the leg (Azevedo et al. 2020). This response is known as a resistance reflex. Resistance reflexes are ubiquitous in limb motor systems of invertebrates and vertebrates, where they help to stabilize the body against external perturbations (Tuthill and Wilson 2016; Tuthill and Azim 2018). In *Drosophila*, the specific FeCO subtypes involved in the resistance reflex of the femur-tibia joint are not known. Our finding that hook axons are not suppressed during passive leg movements (notably also on the treadmill; Video S3) suggests that feedback from hook neurons could mediate this reflex. An advantage of movement over position feedback in this context is that perturbations can be detected more rapidly. Thus, the suppression of hook axons during active leg movements could function to attenuate the resistance reflex, thereby avoiding interference with intended movements. In line with this idea, the activity of hook axons and 9A neurons was consistent across different types of movements: walking, grooming, and other leg movements.

Attenuating reflexes during active movement via presynaptic inhibition may be a common feature of motor systems (McComas 2016). In locusts, stick insects, and crayfish, the axons of chordotonal neurons receive presynaptic inhibition with the potential to suppress resistance reflexes during self-generated movement (Wolf and Burrows 1995; Clarac and Cattaert 1996; Sauer et al. 1997). In mice, the axons of leg proprioceptors receive presynaptic inhibition during walking by a specific class of GABAergic interneurons (Koch et al. 2017). Inactivation of these neurons results in excessive leg flexion, suggesting that presynaptic inhibition functions to suppress resistance reflexes during locomotion. Similarly, mechanosensory neurons of the lateral line system of zebrafish receive presynaptic inhibition during swimming (Pichler and Lagnado 2020; Odstrcil et al. 2022). Inhibition of the lateral line could attenuate rheotaxis, a turning reflex to face into an oncoming current. A potential reason for the widespread occurrence of presynaptic inhibition of sensory axons is the selective control it permits over specific sensory pathways without affecting the operation of postsynaptic circuits.

Behavioral function of sensory transmission in claw axons

We found that hook but not claw axons are suppressed during active leg movements. That is, suppression of feedback is not a general feature of leg proprioception in *Drosophila*, but specific to one proprioceptor subtype. However, like hook axons, claw axons receive primarily GABAergic input and strongly express the $GABA_A$ receptor gene Rdl. The function of this presynaptic inhibition remains unclear, but based on studies in other animals, it could protect the sensory terminals from habituation, sharpen receptive fields through lateral inhibition, or reduce hysteresis in postsynaptic neurons (Clarac and Cattaert 1996).

Overall, claw axons faithfully encoded position signals regardless of the behavioral context. Why are claw axons not suppressed during active leg movements? Claw neurons project to different classes of VNC interneurons (Agrawal et al. 2020; Chen et al. 2021). One possibility is that these interneurons form parallel pathways that support different motor functions. For example, one pathway could mediate a resistance reflex to stabilize posture during resting, while another pathway could ensure proper leg placement during walking and grooming (Dean 1984; Brunn and Dean 1994; Takeoka et al. 2014; Mayer and Akay 2021). In that case, a pathway-specific modulation at the level of interneurons would provide more flexibility than a general modulation at the level of sensory axons. During active movement, the counterproductive resistance reflex pathway could be suppressed without affecting the operation of the leg placement pathway. A similar mechanism is seen in the vestibular system of primates, where sensory axons faithfully relay head movement information regardless of the behavioral context, and pathway-specific modulation occurs at the level of interneurons (Mackrous et al. 2022). A comprehensive analysis of the circuits downstream of claw and hook axons in the VNC connectomes might shed light on the specific pathways for leg motor control.

Predictive inhibition from the brain

The GABAergic 9A interneurons presynaptic to hook axons receive little direct input from sensory neurons and were active only during self-generated movement, synchronously with the predicted sensory signals from hook axons. This suggests that presynaptic inhibition from 9A neurons is predictive of expected proprioceptive feedback. Due to the slow dynamics of GCaMP relative to the speed of fly leg movements, we were unable to determine whether 9A activity precedes movement. However, presynaptic inhibition effectively suppressed hook signals, which would require the presynaptic signal to be predictive in order to overcome sensorimotor delays.

In other mechanosensory systems, inhibition may be graded and dependent on the strength of the movement. In zebrafish, for example, the signal that in-

hibits the mechanosensory neurons of the lateral line system increases with increasing motor activity (Pichler and Lagnado 2020). In the case of 9A neurons, the calcium signals were not correlated with the strength of femur-tibia movement (data not shown). Notably, calcium signals in hook axons are not dependent on the strength of femur-tibia movement either (e.g., joint angle velocity; Mamiya et al. 2018). Rather, hook neurons appear to be active whenever the leg is flexing or extending, regardless of movement speed. Thus, for a predictive signal selectively targeting hook axons, timing is the most important variable. Similarly, predictive signals in other animals seem to match the sensory signals primarily in time when they target early stages of sensory processing (Crapse and Sommer 2008).

If the suppression signal to hook axons is predictive, where is it generated? Predictions of proprioceptive feedback could originate in either low-level motor circuits in the VNC or high-level circuits in the brain. An elegant example of predictive inhibition from low-level motor circuits is found in crickets. When a cricket sings, the sensory axons of its auditory neurons are suppressed by signals from the local motor circuits that produce the singing, thereby allowing the animal to remain sensitive to external sounds (Poulet and Hedwig 2006). Similarly, the axons of leg proprioceptors in mice and locusts are thought to be suppressed by low-level motor circuits that produce walking (Wolf and Burrows 1995; Koch et al. 2017). In the case of 9A neurons, however, predictive inhibition is likely driven by high-level circuits in the brain. The chief 9A neuron, which is the strongest presynaptic partner of hook axons, receives primarily input from descending neurons and little input from local premotor neurons. This circuit motif was stereotyped across two VNC connectomes and was present in all leg neuromeres. In addition, some of the descending neurons targeted several 9A neurons, suggesting they can be recruited together. Evidence for predictive inhibition originating in the brain can be found in other motor systems (McComas 2016). For example, in primates, descending neurons drive the presynaptic inhibition of cutaneous axons during active wrist movements (Seki et al. 2003). Similarly, in zebrafish, an efference copy originating in the hindbrain inhibits the mechanosensory neurons of the lateral line (Pichler and Lagnado 2020; Odstrcil et al. 2022). In weakly electric fish, a cerebellum-like circuit in the brain cancels self-generated electrosensory input during swimming (Wallach and Sawtell 2023).

We found that 9A neurons receive synaptic input from several different descending neurons. The majority of these descending neurons project along one side of the body, suggesting that sensory suppression in hook axons can be regulated in a body-side specific manner. This might be useful for asymmetric behaviors such as turning. Moreover, some descending neurons arborized only within the neuromere of the front leg, while others arborized within the neuromeres of multiple legs, suggesting that sensory suppression can be regulated in a leg-specific manner. Suppressing hook signals from all legs might be useful during behaviors such as walking, when all legs are moving simultaneously. In support of this idea, some of the intersegmental descending neurons presynaptic to the 9A neurons were recently found to drive different aspects of walking (BDN2 and oDN1; Sapkal et al. 2023; DNa02 and DNg13; Yang et al. 2023). In contrast, suppressing hook signals from only a subset of legs might be useful during grooming. During front leg grooming, for example, local descending neurons could drive the suppression of hook signals specifically in front legs, while leaving proprioceptive transmission in the standing middle and hind legs unaffected. Ongoing efforts to bridge the brain and VNC connectomes will soon make it possible to identify these descending neurons in the brain and investigate their connectivity and function.

Conclusion

In this study, we found that proprioceptive movement feedback from the legs is selectively suppressed in behaving *Drosophila*. Selective state-dependent suppression is driven by a segmentally-repeated circuit motif of local GABAergic interneurons and descending neurons that shows signatures of predictive signaling. We propose that the function of this neural circuit is to increase the animal's sensitivity to external perturbations while preventing reflexes from disrupting voluntary movement. In the future, it will be interesting to test whether the same logic extends to analogous movement-encoding (type Ia muscle spindle afferents) and position-encoding (type II muscle spindle afferents) proprioceptors in mammals.

Acknowledgements

We thank members of the Tuthill laboratory for technical assistance and feedback on the manuscript, particularly Anne Sustar for confocal images and Yichen Luo for help with descending neuron identification. We also thank Jan M. Ache, Osama M. Ahmed, Eiman Azim, Eugenia M. Chiappe, and Lydia Zhang for feedback on the manuscript, Jasper S. Phelps, Wei-Chung Allen Lee, and the FANC community for their contributions to the proofreading of the VNC connectome, and James W. Truman for sharing *Drosophila* stocks. We used stocks obtained from the Bloomington *Drosophila* Stock Center (NIH P40OD018537). This work was supported by a Postdoctoral Research Fellowship from the German Research Foundation (DFG) (DA-2322/1-1) to C.J.D, NIH grant K99NS117657 to S.A., as well as a Searle Scholar Award, a Klingenstein-Simons Fellowship, a Pew Biomedical Scholar Award, a McKnight Scholar Award, a Sloan Research Fellowship, the New York Stem Cell Foundation, and NIH grants R01NS102333 and U19NS104655 to J.C.T. J.C.T. is a New York Stem Cell Foundation – Robertson Investigator.

Author contributions

Conceptualization: C.J.D., J.C.T.; data curation: C.J.D.; formal analysis: C.J.D., S.A.; funding acquisition: C.J.D., S.A., J.C.T.; investigation: C.J.D, S.A., A.C.; methodology: C.J.D., S.A.; resources: J.C.T.; software: C.J.D., S.A.; supervision: B.W.B., J.C.T.; visualization: C.J.D.; writing, C.J.D., J.C.T.

Declaration of interests

The authors declare no competing interests.

References

Ache JM, Matheson T (2013) Passive joint forces are tuned to limb use in insects and drive movements without motor activity. *Curr. Biol.* 23:1418–1426.

Agrawal S, Dickinson E, Sustar A, Gurung P, Shepherd D, Truman J, Tuthill J (2020) Central processing of leg proprioception in *Drosophila*. *eLife* 9:e60299.

Azevedo A, Lesser E, Mark B, Phelps J, Elabbady L, Kuroda S, Sustar A, Moussa A, Kandelwal A, Dallmann CJ, Agrawal S, Lee SYJ, Pratt B, Cook A, Skutt-Kakaria K, Gerhard S, Lu R, Kemnitz N, Lee K, Halageri A, Castro M, Ih D, Gager J, Tammam M, Dorkenwald S, Collman F, Schneider-Mizell C, Brittain D, Jordan CS, Dickinson M, Pacureanu A, Seung HS, Macrina T, Lee WCA, Tuthill JC (2022) Tools for comprehensive reconstruction and analysis of *Drosophila* motor circuits. *bioRxiv* p. 2022.12.15.520299.

Azevedo AW, Dickinson ES, Gurung P, Venkatasubramanian L, Mann RS, Tuthill JC (2020) A size principle for recruitment of *Drosophila* leg motor neurons. *eLife* 9:e56754.

Azim E, Seki K (2019) Gain control in the sensorimotor system. *Curr. Opin. Physiol.* 8:177–187.

Bogovic JA, Otsuna H, Heinrich L, Ito M, Jeter J, Meissner G, Nern A, Colonell J, Malkesman O, Ito K, Saalfeld S (2020) An unbiased template of the *Drosophila* brain and ventral nerve cord. *PLoS One* 15:e0236495.

Brunn D, Dean J (1994) Intersegmental and local interneurons in the metathorax of the stick insect *Carausius morosus* that monitor middle leg position. *J. Neurophysiol.* 72:1208–1219.

Bässler U (1993) The femur-tibia control system of stick insects–a model system for the study of the neural basis of joint control. *Brain Res. Rev.* 18:207–226.

Chen C, Agrawal S, Mark B, Mamiya A, Sustar A, Phelps JS, Lee WCA, Dickson BJ, Card GM, Tuthill JC (2021) Functional architecture of neural circuits for leg proprioception in *Drosophila*. *Curr. Biol.* 31:5163–5175.e7.

Chen CL, Hermans L, Viswanathan MC, Fortun D, Aymanns F, Unser M, Cammarato A, Dickinson MH, Ramdya P (2018) Imaging neural activity in the ventral nerve cord of behaving adult *Drosophila*. *Nat. Commun.* 9:4390.

Chockley AS, Dinges GF, Di Cristina G, Ratican S, Bockemühl T, Büschges A (2022) Subsets of leg proprioceptors influence leg kinematics but not interleg coordination in *Drosophila melanogaster* walking. *J. Exp. Biol.* 225:jeb244245.

Clarac F, Cattaert D (1996) Invertebrate presynaptic inhibition and motor control. *Exp. Brain. Res.* 112:163–180.

Crapse TB, Sommer MA (2008) Corollary discharge across the animal kingdom. *Nat. Rev. Neurosci.* 9:587–600.

Cullen KE (2004) Sensory signals during active versus passive movement. *Curr. Opin. Neurobiol.* 14:698–706.

Dallmann CJ, Karashchuk P, Brunton BW, Tuthill JC (2021) A leg to stand on: computational models of proprioception. *Curr. Opin. Physiol.* 22:100426.

Daly KC, Dacks A (2023) The self as part of the sensory ecology: how behavior affects sensation from the inside out. *Curr. Opin. Insect. Sci.* 58:101053.

Dean J (1984) Control of leg protraction in the stick insect: a targeted movement showing compensation for externally applied forces. *J. Comp. Physiol.* 155:771–781.

Dorkenwald S, Schneider-Mizell CM, Brittain D, Halageri A, Jordan C, Kemnitz N, Castro MA, Silversmith W, Maitin-Shephard J, Troidl J, Pfister H, Gillet V, Xenes D, Bae JA, Bodor AL, Buchanan J, Bumbarger DJ, Elabbady L, Jia Z, Kapner D, Kinn S, Lee K, Li K, Lu R, Macrina T, Mahalingam G, Mitchell E, Mondal SS, Mu S, Nehoran B, Popovych S, Takeno M, Torres R, Turner NL, Wong W, Wu J, Yin W, Yu Sc, Reid RC, Da Costa NM, Seung HS, Collman F (2023) CAVE: Connectome annotation versioning engine. *bioRxiv* p. 2023.07.26.550598.

Field LH, Matheson T (1998) Chordotonal organs of insects. *Adv. Insect Physiol.* 27:1–228.

Fink AJ, Croce KR, Huang ZJ, Abbott LF, Jessell TM, Azim E (2014) Presynaptic inhibition of spinal sensory feedback ensures smooth movement. *Nature* 509:43–48.

Frigon A, Akay T, Prilutsky BI (2021) Control of mammalian locomotion by somatosensory feedback. *Compr. Physiol.* 12:2877–2947.

Guizar-Sicairos M, Thurman ST, Fienup JR (2008) Efficient subpixel image registration algorithms. *Opt. Lett.* 33:156–158.

Harris RM, Pfeiffer BD, Rubin GM, Truman JW (2015) Neuron hemilineages provide the functional ground plan for the *Drosophila* ventral nervous system. *eLife* 4:e04493.

Hermans L, Kaynak M, Braun J, Ríos VL, Chen CL, Friedberg A, Günel S, Aymanns F, Sakar MS, Ramdya P (2022) Microengineered devices enable long-term imaging of the ventral nerve cord in behaving adult *Drosophila*. *Nat. Commun.* 13:5006.

Hooper SL, Guschlbauer C, Blümel M, Rosenbaum P, Gruhn M, Akay T, Büschges A (2009) Neural control of unloaded leg posture and of leg swing in stick insect, cockroach, and mouse differs from that in larger animals. *J. Neurosci.* 29:4109–4119.

Karashchuk P, Rupp KL, Dickinson ES, Walling-Bell S, Sanders E, Azim E, Brunton BW, Tuthill JC (2021) Anipose: a toolkit for robust markerless 3d pose estimation. *Cell Rep.* 36:109730.

Koch SC, Del Barrio MG, Dalet A, Gatto G, Günther T, Zhang J, Seidler B, Saur D, Schüle R, Goulding M (2017) RORβ spinal interneurons gate sensory transmission during locomotion to secure a fluid walking gait. *Neuron* 96:1419–1431.e5.

Kuan AT, Phelps JS, Thomas LA, Nguyen TM, Han J, Chen CL, Azevedo AW, Tuthill JC, Funke J, Cloetens P, Pacureanu A, Lee WCA (2020) Dense neuronal reconstruction through X-ray holographic nano-tomography. *Nat. Neurosci.* 23:1637–1643.

Lacin H, Chen HM, Long X, Singer RH, Lee T, Truman JW (2019) Neurotransmitter identity is acquired in a lineage-restricted manner in the *Drosophila* CNS. *eLife* 8:e43701.

Lesser E, Azevedo AW, Phelps JS, Elabbady L, Cook A, Mark B, Kuroda S, Sustar A, Moussa A, Dallmann CJ, Agrawal S, Lee SYJ, Pratt B, Skutt-Kakaria K, Gerhard S, Lu R, Kemnitz N, Lee K, Halageri A, Castro M, Ih D, Gager J, Tammam M, Dorkenwald S, Collman F, Schneider-Mizell C, Brittain D, Jordan CS, Seung HS, Macrina T, Dickinson M, Lee WCA, Tuthill JC (2023) Synaptic architecture of leg and wing motor control networks in *Drosophila*. *bioRxiv* p. 2023.05.30.542725.

Lin S, Hari K, Black S, Khatmi A, Fouad K, Gorassini MA, Li Y, Lucas-Osma AM, Fenrich KK, Bennett DJ (2023) Locomotor-related propriospinal V3 neurons produce primary afferent depolarization and modulate sensory transmission to motoneurons. *J. Neurophysiol.* 130:799–823.

Mackrous I, Carriot J, Cullen K (2022) Context-independent encoding of passive and active self-motion in vestibular afferent fibers during locomotion in primates. *Nat. Commun.* 13:120.

Mamiya A, Gurung P, Tuthill JC (2018) Neural coding of leg proprioception in *Drosophila*. *Neuron* 100:636–650.e6.

Mamiya A, Sustar A, Siwanowicz I, Qi Y, Lu TC, Gurung P, Chen C, Phelps JS, Kuan AT, Pacureanu A, Lee WCA, Li H, Mhatre N, Tuthill JC (2023) Biomechanical origins of proprioceptor feature selectivity and topographic maps in the *Drosophila* leg. *Neuron*. In press.

Marin EC, Morris BJ, Stuerner T, Champion AS, Krzeminski D, Badalamente G, Gkantia M, Dunne CR, Eichler K, Takemura Sy, Tamimi IFM, Fang S, Moon SS, Cheong HSJ, Li F, Schlegel P, Berg S, FlyEM Project Team, Card GM, Costa M, Shepherd D, Jefferis GS (2023) Systematic annotation of a complete adult male *Drosophila* nerve cord connectome reveals principles of functional organisation. *bioRxiv* p. 2023.06.05.543407.

Mathis A, Mamidanna P, Cury KM, Abe T, Murthy VN, Mathis MW, Bethge M (2018) DeepLabCut: markerless pose estimation of user-defined body parts with deep learning. *Nat. Neurosci.* 21:1281–1289.

Mayer WP, Akay T (2021) The role of muscle spindle feedback in the guidance of hindlimb movement by the ipsilateral forelimb during locomotion in mice. *eNeuro* 8:ENEURO.0432–21.2021.

McComas AJ (2016) Hypothesis: Hughlings Jackson and presynaptic inhibition: is there a big picture? *J. Neurophysiol.* 116:41–50.

Meissner GW, Nern A, Dorman Z, DePasquale GM, Forster K, Gibney T, Hausenfluck JH, He Y, Iyer NA, Jeter J, Johnson L, Johnston RM, Lee K, Melton B, Yarbrough B, Zugates CT, Clements J, Goina C, Otsuna H, Rokicki K, Svirskas RR, Aso Y, Card GM, Dickson BJ, Ehrhardt E, Goldammer J, Ito M, Kainmueller D, Korff W, Mais L, Minegishi R, Namiki S, Rubin GM, Sterne GR, Wolff T, Malkesman O, FlyLight Project Team (2023) A searchable image resource of *Drosophila* GAL4 driver expression patterns with single neuron resolution. *eLife* 12:e80660.

Moore RJ, Taylor GJ, Paulk AC, Pearson T, van Swinderen B, Srinivasan MV (2014) FicTrac: A visual method for tracking spherical motion and generating fictive animal paths. *J. Neurosci. Methods* 225:106–119.

Odstrcil I, Petkova MD, Haesemeyer M, Boulanger-Weill J, Nikitchenko M,

Gagnon JA, Oteiza P, Schalek R, Peleg A, Portugues R, Lichtman JW, Engert F (2022) Functional and ultrastructural analysis of reafferent mechanosensation in larval zebrafish. *Curr. Biol.* 32:176–189.e5.

Phelps JS, Hildebrand DGC, Graham BJ, Kuan AT, Thomas LA, Nguyen TM, Buhmann J, Azevedo AW, Sustar A, Agrawal S, Liu M, Shanny BL, Funke J, Tuthill JC, Lee WCA (2021) Reconstruction of motor control circuits in adult *Drosophila* using automated transmission electron microscopy. *Cell* 184:759–774.e18.

Pichler P, Lagnado L (2020) Motor behavior selectively inhibits hair cells activated by forward motion in the lateral line of zebrafish. *Curr. Biol.* 30:150–157.e3.

Plaza S, Clements J, Dolafi T, Umayam L, Neubarth N, Scheffer L, Berg S (2022) neuprint: an open access tool for EM connectomics. *Front. Neuroinform.* 16:896292.

Poulet JFA, Hedwig B (2006) The cellular basis of a corollary discharge. *Science* 311:518–522.

Proske U, Gandevia SC (2012) The proprioceptive senses: their roles in signaling body shape, body position and movement, and muscle force. *Physiol. Rev.* 92:1651–1697.

Rossignol S, Dubuc R, Gossard JP (2006) Dynamic sensorimotor interactions in locomotion. *Physiol. Rev.* 86:89–154.

Rudomin P, Schmidt RF (1999) Presynaptic inhibition in the vertebrate spinal cord revisited. *Exp. Brain Res.* 129:1–37.

Sapkal N, Mancini N, Kumar DS, Spiller N, Murakami K, Vitelli G, Bargeron B, Maier K, Eichler K, Jefferis GS, Shiu PK, Sterne GR, Bidaye SS (2023) Neural circuit mechanisms underlying context-specific halting in *Drosophila*. *bioRxiv* p. 2023.09.25.559438.

Sauer A, Büschges A, Stein W (1997) Role of presynaptic inputs to proprioceptive afferents in tuning sensorimotor pathways of an insect joint control network. *J. Neurobiol.* 32:359–376.

Schindelin J, Arganda-Carreras I, Frise E, Kaynig V, Longair M, Pietzsch T, Preibisch S, Rueden C, Saalfeld S, Schmid B, Tinevez JY, White DJ, Hartenstein V, Eliceiri K, Tomancak P, Cardona A (2012) Fiji: an open-source platform for biological-image analysis. *Nat. Methods* 9:676–682.

Seki K, Perlmutter SI, Fetz EE (2003) Sensory input to primate spinal cord is presynaptically inhibited during voluntary movement. *Nat. Neurosci.* 6:1309–1316.

Straka H, Simmers J, Chagnaud B (2018) A new perspective on predictive motor signaling. *Curr. Biol.* 28:R232–R243.

Takemura Sy, Hayworth KJ, Huang GB, Januszewski M, Lu Z, Marin EC, Preibisch S, Xu CS, Bogovic J, Champion AS, Cheong HS, Costa M, Eichler K, Katz W, Knecht C, Li F, Morris BJ, Ordish C, Rivlin PK, Schlegel P, Shinomiya K, Stürner T, Zhao T, Badalamente G, Bailey D, Brooks P, Canino BS, Clements J, Cook M, Duclos O, Dunne CR, Fairbanks K, Fang S, Finley-May S, Francis A, George R, Gkantia M, Harrington K, Hopkins GP, Hsu J, Hubbard PM, Javier A, Kainmueller D, Korff W, Kovalyak J, Krzemiński D, Lauchie SA, Lohff A, Maldonado C, Manley EA, Mooney C, Neace E, Nichols M, Ogundeyi O, Okeoma N, Paterson T, Phillips E, Phillips EM, Ribeiro C, Ryan SM, Rymer JT, Scott AK, Scott AL, Shepherd D, Shinomiya A, Smith C, Smith N, Suleiman A, Takemura S, Talebi I, Tamimi IF, Trautman ET, Umayam L, Walsh JJ, Yang T, Rubin GM, Scheffer LK, Funke J, Saalfeld S, Hess HF, Plaza SM, Card GM, Jefferis GS, Berg S (2023) A connectome of the male *Drosophila* ventral nerve cord. *bioRxiv* p. 2023.06.05.543757.

Takeoka A, Vollenweider I, Courtine G, Arber S (2014) Muscle spindle feedback directs locomotor recovery and circuit reorganization after spinal cord injury. *Cell* 159:1626–1639.

Tuthill JC, Azim E (2018) Proprioception. *Curr. Biol.* 28:R194–R203.

Tuthill JC, Wilson RI (2016) Mechanosensation and adaptive motor control in insects. *Curr. Biol.* 27:R1022–R1038.

Wallach A, Sawtell NB (2023) An internal model for canceling self-generated sensory input in freely behaving electric fish. *Neuron* 111:2570–2582.e5.

Weir PT, Dickinson MH (2015) Functional divisions for visual processing in the central brain of flying *Drosophila*. *Proc. Natl. Acad. Sci. U.S.A.* 112:E5523–E5532.

Wolf H, Burrows M (1995) Proprioceptive sensory neurons of a locust leg receive rhythmic presynaptic inhibition during walking. *J. Neurosci.* 15:5623–5636.

Yang HH, Brezovec LE, Capdevila LS, Vanderbeck QX, Rayshubskiy S, Wilson RI (2023) Fine-grained descending control of steering in walking *Drosophila*. *bioRxiv* p. 2023.10.15.562426.

Methods

Resource availability

Lead contact. Further information and requests for resources and reagents should be directed to and will be fulfilled by the lead contact, John C. Tuthill (tuthill@uw.edu).

Materials availability. The split-GAL4 driver lines used in this study are available upon request from the lead contact. The underlying AD and DBD lines are listed in the key resources table and are available from the Bloomington *Drosophila* Stock Center or the lead contact.

Data and code availability. Calcium imaging and behavioral data generated for this paper will be available for download from Dryad. Data from the FANC connectome was analyzed from the CAVE materialization version 721, timestamp 2023-09-21T08:10:01.216565. Analysis code used in this study will be available on GitHub (https://github.com/tuthill-lab). Any additional information required to reanalyze the data is available from the lead contact upon request.

Experimental animals

We used *Drosophila melanogaster* raised on standard cornmeal and molasses medium at 25℃ in a 14:10 hour light:dark cycle. We used male flies 1 to 6 days post-eclosion for imaging experiments, except for the fully constrained preparation (Figure S5) where we used female flies. The genotypes used for each experiment are listed in a table below.

Sample preparation for confocal imaging of the VNC

For confocal imaging of FeCO axons and 9A neurons in the VNC, we crossed flies carrying the GAL4 driver to flies carrying pJFRC7-20XUAS-IVS-mCD8::GFP and dissected the VNC of females out of the thorax in *Drosophila* saline (103 mM NaCl, 3 mM KCl, 5 mM TES, 8 mM trehalose, 10 mM glucose, 26 mM NaHCO3, 1 mM NaH2PO4, 1.5 mM CaCl2, and 4 mM MgCl2; pH 7.1; osmolality adjusted to 270-275 mOsm). We fixed the VNC in a 4% paraformaldehyde PBS solution for 15 min. Next, we rinsed the VNC in PBS three times and put it in blocking solution (5% normal goat serum in PBS with 0.2% Triton-X) for 20 min, and then incubated it with a solution of primary antibody (rat anti-CD8 antibody, 1:50 concentration; mouse anti-Bruchpilot antibody for neuropil staining, 1:50 concentration) dissolved in blocking solution for 24 hours at room temperature. At the end of the first incubation, we washed the VNC with PBS with 0.2% Triton-X (PBST) three times, and then incubated the VNC in a solution of secondary antibody (goat anti-rat antibody Alexa Fluor 488, 1:250 concentration; goat anti-mouse antibody Alexa Fluor 633, 1:250 concentration) dissolved in blocking solution for 24 hours at room temperature. Finally, we washed the VNC in PBST three times and then mounted it on a

slide with Vectashield (Vector Laboratories). We acquired z-stacks of each VNC on a confocal microscope (Zeiss 510; Zeiss). We aligned the expression pattern in the VNC using the Computational Morphometry Toolkit (CMTK; Neuroimaging Informatics Tools and Resources Clearinghouse) to a female VNC template (Bogovic et al. 2020) in Fiji (Schindelin et al. 2012).

Fly preparation for *in vivo* two-photon calcium imaging in the VNC

For recording calcium signals in the VNC of behaving flies, we adapted a previously described preparation (Chen et al. 2018; Hermans et al. 2022). First, we clipped the fly's wings under cold anesthesia. Then, we pushed the dorsal part of the thorax through a hole (0.8 mm width, 0.95 mm length) in a curved steel sheet at the bottom side of a custom-made holder. The thorax was fixed using UV-curing glue (KOA 300; Kemxert) applied around the perimeter of the thorax on the top side of the holder. This left the fly's legs, head, and abdomen on the bottom side of the holder free to move. The top side of the holder was then immersed in *Drosophila* saline. To gain optical access to the VNC, a rectangular piece of cuticle was removed from the dorsal thorax. This exposed the indirect flight muscles (IFMs) while leaving the body-wall muscles intact. IFMs were parted along the midline of the body using a tapered insect pin (0.1 mm diameter; Living Systems Instrumentation). We waited ~60 min for IFMs to partly dissolve. Remaining IFMs were then removed using the insect pin. Removing IFMs exposed the proventriculus (or cardia, a part of the gut) and surrounding tracheae above the neuromeres of the front legs. Fine forceps were used to pull out the anterior trachea above the neck connective and remove the underlying fat bodies. Then, the proventriculus was moved to the right side of the thorax using an insect pin, exposing most of the neuromere of the left front leg. The pin was held in place by a sculpting compound (Super Sculpey Firm) positioned next to the thorax. A second insect pin was inserted into the sculpting compound and thorax to displace the left lateral trachea. Care was taken not to touch the VNC while displacing the gut and tracheae. Leaving the gut and tracheae intact proved critical for normal fly behavior and allowed us to record from the VNC for several hours. After the dissection, the fly holder was mounted onto a three-axis manipulator, and the fly was positioned above the treadmill. We typically gave flies 30-60 min to recover from the preparation before starting the experiments.

For recording calcium signals in the VNC while controlling tibia position with the magnet-motor system (see below), we used a previously described preparation in which the fly is oriented ventral side up (Mamiya et al. 2018). We first cold anesthetized the fly on ice and then pushed the head and ventral thorax through a hole in a steel sheet of a custom-made holder. The head and thorax were fixed using UV-curing glue (KOA 300; Kemxert). The abdomen and legs were placed on the bottom side of the holder. To control the femur-tibia joint angle, we glued the femur of the right front leg to the bottom side of the holder and attached a small piece of insect pin (~1 mm length, 0.1 mm diameter; Living Systems Instrumentation) to the tibia and tarsus. The pin was painted black (Super Black; Speedball Art Products) to improve image contrast for movement tracking (see below). All other legs were glued to the holder to not interfere with the movement of the tibia of the right front leg. The top side of the holder was then immersed in *Drosophila* saline. To gain optical access to the VNC, the cuticle covering the front leg neuromeres was removed with fine forceps. Fat bodies and larger trachea covering the imaging region of interest were removed as well. Finally, we removed the digestive tract with fine forceps to reduce the movement of the VNC.

In vivo two-photon image acquisition

For recording calcium signals in the VNC during behavior and motor-controlled movements of the tibia, we used two two-photon Movable Objective Microscopes (MOM; Sutter Instruments) with a 20x water-immersion objective (Olympus XLUMPlanFI, 0.95 NA, 2.0 mm wd; Olympus) and a 40x water-immersion objective (0.8 NA, 2.0 mm wd; Nikon Instruments), respectively. Neurons of interest expressed the calcium indicator GCaMP6f or GCaMP7f (green fluorescence) and the structural marker tdTomato (red fluorescence). Fluorophores were excited at 920 nm by a mode-locked Ti:sapphire laser (Chameleon Vision S; Coherent). We used a Pockels cell to keep the power at the back aperture of the objective below ~35 mW. Emitted fluorescence was directed to two high-sensitivity GaAsP photomultiplier tubes (Hamamatsu Photonics) through a 705 nm edge dichroic beamsplitter followed by a 580 nm edge image-splitting dichroic beamsplitter (Semrock). Fluorescence was band-passed filtered by either a 525/50 (green) or 641/75 (red) emission filter (Semrock). Image acquisition was controlled with ScanImage 5.2 (Vidrio Technologies) in Matlab (MathWorks). Each microscope was equipped with a galvo-resonant scanner, and each objective was mounted onto a piezo actuator (Physik Instrumente; digital piezo controller E-709). For recordings during behavior, we acquired volumes of three 512 x 512 pixel images spaced 5 µm apart in depth (10 µm total) at a speed of 8.26 volumes per second. We typically recorded 400 volumes (~50 s) per trial. For recordings during motor-controlled movements of the tibia, we acquired volumes of three 256 x 128 pixel images spaced 10 µm apart in depth (20 µm total) at a speed of 36.7 volumes per second. Previous experiments revealed that calcium signals in claw and hook axons do not differ qualitatively across different axon branches when the leg is passively moved (Mamiya et al. 2018). Therefore, we focused our experiments on a single imaging region. All experiments were performed in the dark at room temperature.

Two-photon GCaMP and tdTomato image analysis

Two-photon images were analyzed with custom scripts in Matlab. Images acquired during behavior were analyzed in nine steps. First, we smoothed each image with a Gaussian filter (sigma = 3 pixels; size = 5 x 5 pixels). Second, we corrected for horizontal movement of the VNC. Each tdTomato image was aligned to the average tdTomato signal of the recorded trial via translations using a cross-correlation-based image registration algorithm (upsampling factor = 4; Guizar-Sicairos et al. 2008). The same translations were then applied to the GCaMP images. Third, the three GCaMP and tdTomato images per volume were averaged. Fourth, we extracted the mean fluorescence in manually drawn regions of interest (ROIs). Fifth, we corrected for vertical movement of the VNC by computing the ratio of GCaMP fluorescence to tdTomato fluorescence in each frame (Weir and Dickinson 2015). Dividing the GCaMP fluorescence by the tdTomato fluorescence decreased the impact of vertical movement, because such movements result in correlated changes in both signals, and the tdTomato signal is independent of neural activity. Sixth, to facilitate comparisons across trials and flies, ratio values were z-scored by subtracting the mean of a baseline ratio and dividing by the standard deviation of that baseline ratio. The baseline was defined in each trial as the 10% smallest ratio values. Seventh, z-scored ratio values were upsampled to the sampling rate of leg tracking (300 Hz) using cubic spline interpolation. Eighth, upsampled ratio values were low-pass filtered using a moving average filter with a time window of 0.2 s. Ninth, to facilitate comparisons with predicted calcium values, we normalized the measured calcium values to be between zero and one by dividing each z-scored ratio value by the maximum z-scored ratio value for a given genetic driver line in the dataset.

Two-photon images acquired during motor-controlled movements of the tibia (Figure S5) were analyzed similarly, but due to a lack of VNC movement in that setup, correcting for horizontal and vertical movement of the VNC (steps 2 and 5 above) was not necessary. Instead, we computed the change in GCaMP fluorescence relative to a baseline per trial. For each frame, we subtracted the mean of the baseline from the GCaMP fluorescence and divided by the mean of the baseline. The baseline was defined per trial as the lowest average GCaMP fluorescence in a window of 0.27 s (10 frames). Then, calcium signals were z-scored, upsampled, low-pass filtered, and normalized as described above (steps 6–9).

To fit the computational models (see below), we z-scored and normalized the calcium imaging data from Mamiya et al. (2018) in the same manner as the data recorded from behaving flies. That is, we first z-scored the calcium signals per trial relative to a baseline, and then divided each z-scored value by the maximum z-scored value for a given genetic driver line in the dataset.

Treadmill

The omnidirectional treadmill consisted of a patterned Styrofoam ball (9.1 mm diameter; 0.12 g) floating on air in an aluminum holder. The air flow was set to 500 ml/min. The ball was illuminated by two infrared LEDs (850-nm peak wavelength; ThorLabs) via optical fibers. Ball movements were recorded with a camera at 30 Hz (Basler acA1300-200µm; Basler AG) equipped with a macro zoom lens (Computar MLM3X-MP; Edmund Optics). Ball rotations around the fly's cardinal body axes (forward, rotational, sideward) were reconstructed offline using FicTrac (Moore et al. 2014). Rotational velocities of the fly were calculated based on the known diameter of the ball. Velocities were upsampled to the sampling rate of leg tracking (300 Hz) using cubic spline interpolation and low-pass filtered using a moving average filter with a time window of 0.2 s. The treadmill was mounted onto a one-axis manipulator. This allowed us to remove the treadmill in between trials and record data for leg movements in the air or on the platform.

Platform for moving the leg

The platform consisted of a metal pin (0.5 mm diameter, 4.4 mm length) mounted onto a three-axis micromanipulator (MP-225; Sutter Instruments). The pin was wrapped in black sandpaper to provide sufficient grip for the flies' tarsi. The micromanipulator was controlled manually.

Magnet-motor system for moving the tibia

We used a previously described magnet-motor system (Mamiya et al. 2018) to control the femur-tibia angle during calcium imaging. We moved the tibia/pin to different positions via a cylindrical rare earth magnet (10 mm height, 5 mm diameter). The magnet was attached to a steel post whose position was controlled with a programmable servo motor (SilverMax QCI-X23C-1; QuickSilver Controls). The motor was mounted onto a micromanipulator (MP-225; Sutter Instruments). This allowed us to adjust the motor position so that the magnet moved in a circular trajectory centered at the femur-tibia joint.

The movement of the magnet, and with that, the tibia, was controlled with a custom script in Matlab. We imposed movements that were representative of femur-tibia joint angles and velocities recorded during walking and grooming (Figure S5B). Each trial started at a femur-tibia angle of ~90°. In "walking" trials, we replayed 67 movement bouts containing different front leg walking kinematics. Each bout was 2 s in duration. In "grooming" trials, we replayed 12 movement bouts containing different front leg grooming kinematics. Bout durations ranged from 0.3 s to 2 s. Because movement bouts did not necessarily start or end at a femur-tibia angle of 90°, we added a 0.25 s transition phase before and after each bout, in which the tibia was linearly moved to the start position or back to 90°. The tibia was not moved for 0.5 s in between stimuli.

Tracking of the femur-tibia joint

For recordings during behavior, movements of the left front leg were recorded at 300 Hz with two cameras (Basler acA800-510µm; Basler AG) equipped with 1.0x InfiniStix lenses (68 mm wd; Infinity) and 875 nm short pass filters (Edmund Optics). The leg was illuminated by an infrared LED (850-nm peak wavelength; ThorLabs) via an optical fiber. We trained a deep neural network (DeepLabCut; Mathis et al. 2018) to automatically track all leg joints in each camera view. 2D tracking data from both camera views were then combined to reconstruct leg joint positions and angles in 3D using Anipose (Karashchuk et al. 2021). Specifically, we applied a median filter on the 2D tracking data and then used spatiotemporally regularized triangulation. The two cameras were calibrated using a ChArUco board (6x6 markers, 4 bits per marker, 0.125 mm marker length). 3D leg tracking was necessary to provide accurate femur-tibia joint angle information for the computational models that predicted calcium signals in our neurons of interest (see below).

For recordings with the magnet-motor system, movements of the right front leg tibia were recorded at 200 Hz with a single camera (Basler acA800-510µm; Basler AG) equipped with a 1.0x InfiniStix lens (94 mm wd; Infinity) and a 900 nm short pass filter (Edmund Optics). Because the servo motor was placed directly under the fly, we placed the camera to the side and used a prism (Edmund Optics) to capture the view from below. The leg was illuminated by an infrared LED (850-nm peak wavelength; ThorLabs) via an optical fiber. The coxa-femur, femur-tibia, and tibia-tarsus joints were tracked using DeepLabCut. Because the tibia moved in a single plane parallel to the surface of the holder, 2D tracking was sufficient to provide accurate femur-tibia joint angle information for the computational models.

Data annotations and data selection

For trials involving the treadmill and platform, fly behavior was classified semi-automatically based on the leg tracking data. All classifications were reviewed and manually corrected if necessary. First, movement of the left front leg was determined based on the speed of the leg's tarsus in the side-view camera. The velocity was low-pass filtered using a moving average filter with a time window of 0.3 s. Frames in which the velocity exceeded 0.8 px/s were classified as moving. The resulting binary behavioral sequence was low-pass filtered by removing epochs shorter than 250 ms (hysteresis filter). That is, the behavioral sequence could only change state if at least 250 ms were in a new state. In trials involving the treadmill, movements were further classified as walking or grooming based on the movement of the left middle leg. Movement of the middle leg was determined analogously to that of the front leg (low-pass filter followed by thresholding and hysteresis filter). Epochs in which both the front leg and the middle leg moved were classified as walking. Epochs in which the front leg but not the middle leg moved were classified as front leg grooming. Front leg movements other than walking or grooming were manually classified as "other."

For trials involving the platform, we additionally manually annotated periods of passive leg movement based on the leg videos. For hook flexion neurons, we annotated passive flexions of the femur-tibia joint (Figure 3G). For hook extension neurons, we annotated passive extensions of the femur-tibia joint (Figure S4H). For 9A neurons, we annotated all passive movements of the leg (Figure 4H).

Frames were manually excluded from the analysis if the front leg was involved in movements other than walking or grooming on the treadmill (e.g., ball pushing), the femur-tibia joint of the front leg was not tracked correctly, or the two-photon image registration failed (e.g., the VNC moved out of the imaging volume). When calculating the cross-correlation for passive leg movements with the platform, we additionally excluded frames in which the leg moved actively. Behavioral bouts and movement transitions were excluded if they were shorter than the desired minimum duration (see figure legends).

For some genotypes (see table of genotypes below), we recorded neural activity with GCaMP6f and GCaMP7f. We did not observe any differences in the calcium signals and therefore pooled recordings for our analysis.

Computational models for predicting calcium signals in neurons

We constructed computational models to predict time courses of calcium signals in claw, hook, and 9A neurons from time courses of femur-tibia joint kinematics. The joint kinematics were fed into a neuron type-specific activation function, which was convolved with a double exponential function to mimic the temporal dynamics of GCaMP:

$$e^{-t/\tau_{off}} - e^{-t/\tau_{on}},$$

with an onset time constant τ_{on} = 0.03 s and an offset time constant τ_{off} = 0.3 s. The time constants were tuned to match the measured calcium signals in claw and hook axons in Mamiya et al. (2018) (Figure S2).

The activation functions for claw and hook neurons were based on calcium imaging and leg tracking data from Mamiya et al. (2018), where the femur-tibia joint was passively moved using ramp-and-hold stimuli (Figure S2). In that dataset, calcium signals in claw axons are lowest at a joint angle of 90° and increase nonlinearly with increasing flexion or extension. To model this encoding, we first subtracted 90° from the tracked femur-tibia joint angle. Then, we fitted a 4th order polynomial activation function (convolved with the GCaMP kernel) to the z-scored and normalized calcium signals using nonlinear least-squares optimization (lsqcurvefit; Matlab; Figure S2A). In our dataset, calcium signals

were weakest at a joint angle of 80° (Figure 2F). Thus, for our dataset, we subtracted 80° from the tracked femur-tibia joint angle, but used the same activation function. The 10° difference between the datasets is likely related to differences in leg tracking, not encoding.

Hook neurons were assumed to encode flexion or extension direction. To model this encoding, the joint angle velocity was fed into a binary step function (Figure S2A). For hook flexion neurons, we used a threshold of -5 deg/s for the dataset from Mamiya et al. (2018) and -50 deg/s for our dataset. Different thresholds were chosen to account for different amounts of tracking noise in the datasets. Mamiya et al. (2018) did not test hook extension neurons. But based on Mamiya et al. (2023), hook extension neurons have the opposite encoding of hook flexion neurons, which we modeled with a binary step function with a threshold of 50 deg/s in our dataset (Figure S2A).

To model activity of 9A neurons, which we assumed respond during active (but not passive) flexion and extension, the joint angle velocity was fed into a rectangular function with thresholds of $\pm$50 deg/s (Figure S2A). For times when the leg was passively moved, the joint angle velocity input was set to zero.

To facilitate comparisons with measured calcium values, we normalized the predicted calcium values to be between zero and one by subtracting the minimum predicted value in each trial and dividing by the maximum predicted value for a given genetic driver line in the dataset.

Reconstruction of FeCO axons and presynaptic neurons in the FANC connectome

Neurons in the Female Adult Nerve Cord (FANC) electron microscopy dataset (Phelps et al. 2021) were previously segmented in an automated manner (Azevedo et al. 2022). To manually correct the automated segmentation of claw and hook axons and their presynaptic neurons, we used Google's collaborative Neuroglancer interface. Pre- and postsynaptic neurons that made less than three synapses with a neuron of interest were excluded from connectivity analyses. Neuron annotations were managed by the Connectome Annotation Versioning Engine (CAVE; Dorkenwald et al. 2023). We used custom scripts in Python to interact with CAVE via CAVEclient (Dorkenwald et al. 2023) and analyze connectivity.

Identification of hemilineages and fast-acting neurotransmitters

In *Drosophila*, neurons that share a developmental origin (i.e., belong to the same hemilineage) possess common anatomical features (Harris et al. 2015) and release the same fast-acting neurotransmitter (GABA, glutamate, or acetylcholine; Lacin et al. 2019). We took advantage of this knowledge to identify the hemilineage and thus the fast-acting neurotransmitter of each VNC neuron presynaptic to the claw and hook axons in the FANC connectome. For identification, we relied on light microscopy images of sparse GAL4 lines, cell body position along the dorsal-ventral axis (Lacin et al. 2019; Meissner et al. 2023), and personal communication (James W. Truman, David Shepherd, Haluk Lacin, and Elizabeth Marin).

Definition of cell classes

Neurons presynaptic to the 9A interneurons were identified as sensory neurons, descending neurons, or premotor neurons. Sensory neurons had processes entering the VNC from peripheral nerves and no cell body in the VNC. Descending neurons had a process in the neck connective and no cell body in the VNC. Premotor neurons were presynaptic to leg motor neurons in the neuromere of the left front leg. These neurons were previously annotated in FANC by Lesser et al. (2023).

Circuit analysis in the MANC connectome

The Male Adult Nerve Cord (MANC) connectome (Takemura et al. 2023) and its annotations (Marin et al. 2023) were queried via the NeuPrint API and web explorer (Plaza et al. 2022).

Key resources table

Reagent or resource	Source	Identifier
Antibodies		
Mouse anti-Bruchpilot monoclonal antibody	Developmental Studies Hybridoma Ban	RRID:AB_2314866
Rat anti-CD8 monoclonal antibody	Thermo Fisher Scientific	RRID:AB_10392843
Goat anti-mouse secondary antibody, Alexa Fluor 633 conjugate	Invitrogen	RRID:AB_141431
Goat anti-rat secondary antibody, Alexa Fluor 488 conjugate	Thermo Fisher Scientific	RRID:AB_2534074
Deposited data		
Calcium imaging data of FeCO axons during simple passive leg movements	Mamiya et al. (2018)	https://faculty.washington.edu/tuthill/publications.html
RNA-sequencing dataset of FeCO neurons	Mamiya et al. (2023)	GEO:GSE236232
FANC connectome	Azevedo et al. (2022)	https://fanc.community
MANC connectome	Takemura et al. (2023)	https://neuprint.janelia.org
Experimental models: Organisms/strains		
P{y[+t7.7] w[+mC]=20XUAS-IVS-mCD8::GFP}attP2	Bloomington	RRID:BDSC_32194
P{y[+t7.7] w[+mC]=20XUAS-IVS-GCaMP6f}attP40; P{w[+mC]=UAS-tdTom.S}3	Gift from Peter Weir and Michael Dickinson, Caltech	N/A
P{w[+mC]=UAS-tdTom.S}2	Bloomington	RRID:BDSC_36327
PBac{y[+mDint2] w[+mC]=20XUAS-IVS-jGCaMP7f}VK00005	Bloomington	RRID:BDSC_79031
P{w[+mc]=iav-GAL4.K}3	Bloomington	RRID:BDSC_52273
P{y[+t7.7] w[+mC]=GMR73D10-GAL4}attP2	Bloomington	RRID:BDSC_39819
P{y[+t7.7] w[+mC]=GMR21D12-GAL4}attP2	Bloomington	RRID:BDSC_48946
P{y[+t7.7] w[+mC]=VT038873-p65AD}attP40	Gift from Barry J. Dickson, Janelia Farm, HHMI	N/A
P{y[+t7.7] w[+mC]=R32H08-GAL4.DBD}attP2	Bloomington	RRID:BDSC_69119
P{y[+t7.7] w[+mC]=VT018774-p65AD}attP40	Bloomington	RRID:BDSC_93430
P{y[+t7.7] w[+mC]=VT040547-GAL4.DBD}attP2	Gift from Barry J. Dickson, Janelia Farm, HHMI	N/A
P{y[+t7.7] w[+mC]=R12C09-GAL4.AD}attP40	Gift from James W. Truman, University of Washington	N/A
P{y[+t7.7] w[+mC]=R30A10-GAL4.DBD}attP2	Gift from James W. Truman, University of Washington	N/A
Software and algorithms		
Anipose	Karashchuk et al. (2021)	RRID:SCR_023041
CAVEclient	Dorkenwald et al. (2023)	https://github.com/seung-lab/CAVEclient
Computational Morphometry Toolkit	Neuroimaging Informatics Tools and Resources Clearinghouse	https://www.nitrc.org/projects/cmtk/
DeepLabCut	Mathis et al. (2018)	RRID:SCR_021391
FicTrac	Moore et al. (2014)	https://github.com/rjdmoore/fictrac

FIJI	Schindelin et al. (2012)	RRID:SCR_002285
Matlab	MathWorks	RRID:SCR_001622
neuPrint	Plaza et al. (2022)	https://neuprint.janelia.org/
Neuroglancer		RRID:SCR_015631
ScanImage 5.2	Vidrio Technologies	RRID:SCR_014307

Table of genotypes

Figure 1B, left: FeCO neurons expressing GFP in the leg	+ / +; P{y[+t7.7] w[+mC]=20XUAS-IVS-mCD8::GFP}attP2 / P{w[+mc]=iav-GAL4.K}3
Figure 1B, right: claw neurons expressing GFP	+ / +; P{y[+t7.7] w[+mC]=20XUAS-IVS-mCD8::GFP}attP2 / P{y[+t7.7] w[+mC]=GMR73D10-GAL4}attP2
Figure 1B, right: hook flexion neurons expressing GFP	+ / +; P{y[+t7.7] w[+mC]=20XUAS-IVS-mCD8::GFP}attP2; P{y[+t7.7] w[+mC]=GMR21D12-GAL4}attP2
Figure 1B, right: hook extension neurons expressing GFP	+ / P{y[+t7.7] w[+mC]=VT018774-p65AD}attP40; P{y[+t7.7] w[+mC]=20XUAS-IVS-mCD8::GFP}attP2 / P{y[+t7.7] w[+mC]=VT040547-GAL4.DBD}attP2;
Figure 2, S2: claw neurons expressing tdTomato and GCaMP7f	P{w[+mC]=UAS-tdTom.S}2 / +; PBac{y[+mDint2] w[+mC]=20XUAS-IVS-jGCaMP7f}VK00005 / P{y[+t7.7] w[+mC]=GMR73D10-GAL4}attP2
Figure 2, S2: claw neurons expressing GCaMP6f and tdTomato	P{y[+t7.7] w[+mC]=20XUAS-IVS-GCaMP6f}attP40 / +; P{w[+mC]=UAS-tdTom.S}3 / P{y[+t7.7] w[+mC]=GMR73D10-GAL4}attP2
Figure 3, S3, S5: hook flexion neurons expressing tdTomato and GCaMP7f	P{w[+mC]=UAS-tdTom.S}2 / +; PBac{y[+mDint2] w[+mC]=20XUAS-IVS-jGCaMP7f}VK00005 / P{y[+t7.7] w[+mC]=GMR21D12-GAL4}attP2
Figure 4, S7: 9A neurons expressing tdTomato and GCaMP7f	P{w[+mC]=UAS-tdTom.S}2 / P{y[+t7.7] w[+mC]=R30A10-GAL4.DBD}attP2; PBac{y[+mDint2] w[+mC]=20XUAS-IVS-jGCaMP7f}VK00005 / P{y[+t7.7] w[+mC]=R12C09-GAL4.AD}attP40
Figure S3, driver line 2: hook flexion neurons expressing tdTomato and GCaMP7f	P{w[+mC]=UAS-tdTom.S}2 / P{y[+t7.7] w[+mC]=VT038873-p65AD}attP40; PBac{y[+mDint2] w[+mC]=20XUAS-IVS-jGCaMP7f}VK00005 / P{y[+t7.7] w[+mC]=R32H08-GAL4.DBD}attP2
Figure S3, driver line 2: hook flexion neurons expressing GCaMP6f and tdTomato	P{y[+t7.7] w[+mC]=20XUAS-IVS-GCaMP6f}attP40 / P{y[+t7.7] w[+mC]=VT038873-p65AD}attP40; P{w[+mC]=UAS-tdTom.S}3 / P{y[+t7.7] w[+mC]=R32H08-GAL4.DBD}attP2
Figure S4: hook extension neurons expressing tdTomato and GCaMP7f	P{w[+mC]=UAS-tdTom.S}2 / P{y[+t7.7] w[+mC]=VT018774-p65AD}attP40; PBac{y[+mDint2] w[+mC]=20XUAS-IVS-jGCaMP7f}VK00005 / P{y[+t7.7] w[+mC]=VT040547-GAL4.DBD}attP2

Supplementary figures

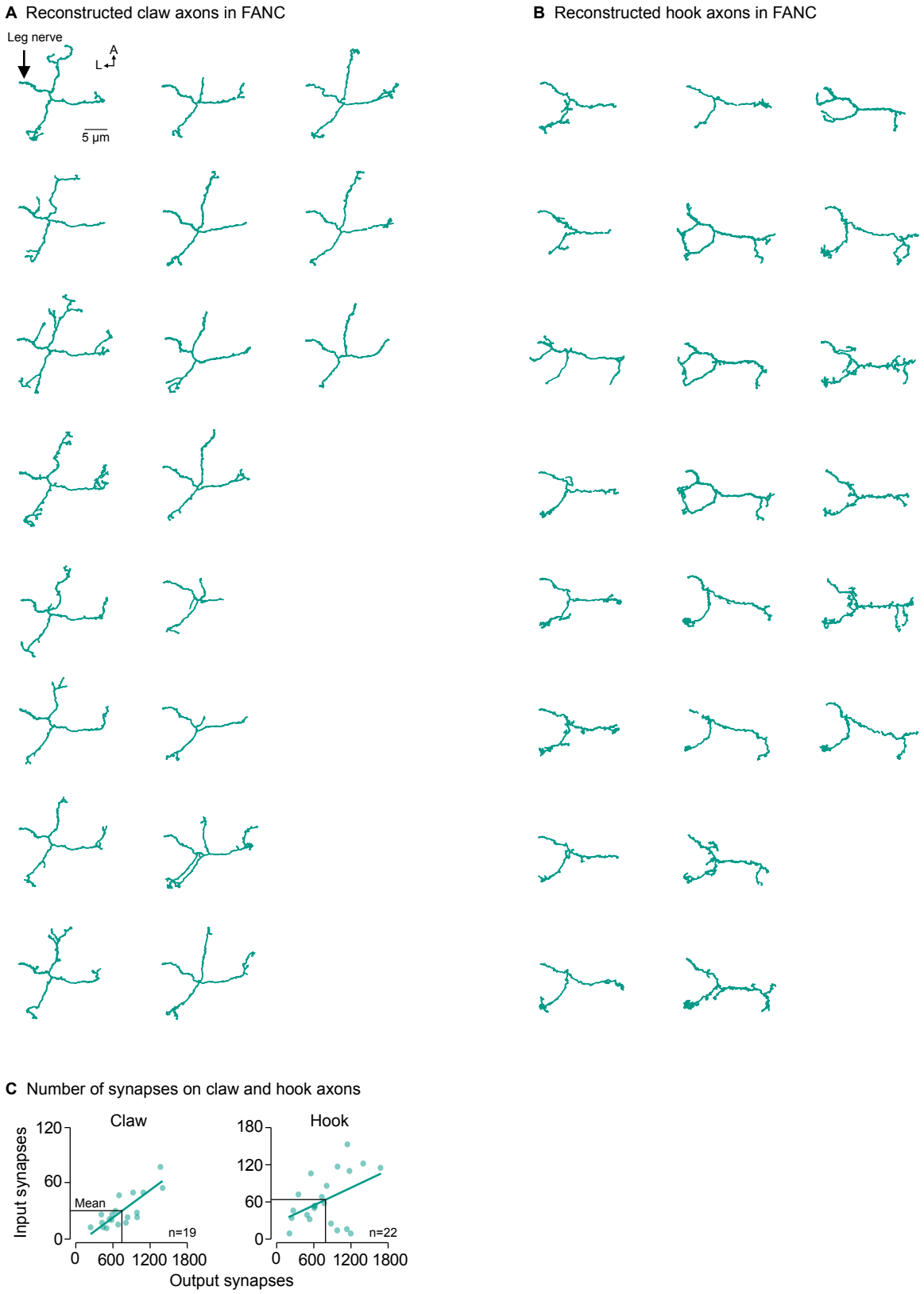

Figure S1.

(A) Top view of reconstructed claw axons in the left front leg neuromere of the FANC connectome. A: anterior; L: lateral.

(B) Top view of reconstructed hook axons in the left front leg neuromere of the FANC connectome. View as in (A).

(C) Number of input and output synapses for individual claw and hook axons. Black lines indicate the mean. Green lines indicate linear fits. n: number of axons.

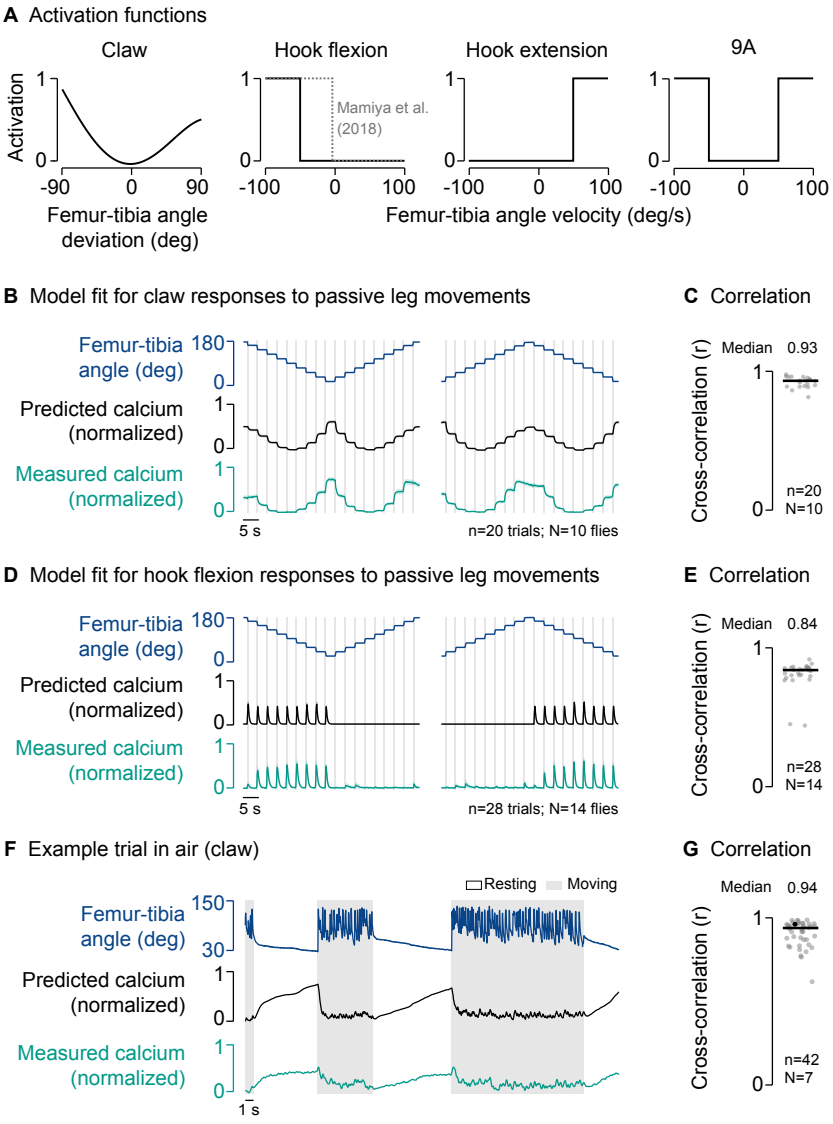

Figure S2.
(A) Activation functions for claw, hook flexion, hook extension, and 9A neurons.
(B) Measured and predicted (fitted) calcium signals of claw axons in response to applied ramp-and-hold movements of the femur-tibia joint. Experimental data from Mamiya et al. (2018). Lines show mean of animal means, shadings show standard error of the mean. n: number of trials (10 trials per ramp-and-hold stimulus, totalling 20 trials for both stimuli); N: number of flies.
(C) Cross-correlation coefficient between predicted and measured calcium signals per trial at a time lag of zero. The black line shows the median. n: number of trials; N: number of flies.
(D) Same as (B) but for hook flexion axons.
(E) Same as (C) but for hook flexion axons.
(F) Example trial of two-photon calcium imaging of claw axons and behavior tracking without the treadmill.
(G) Same as (C) but for claw axons imaged without the treadmill. The black dot marks the trial shown in (F).

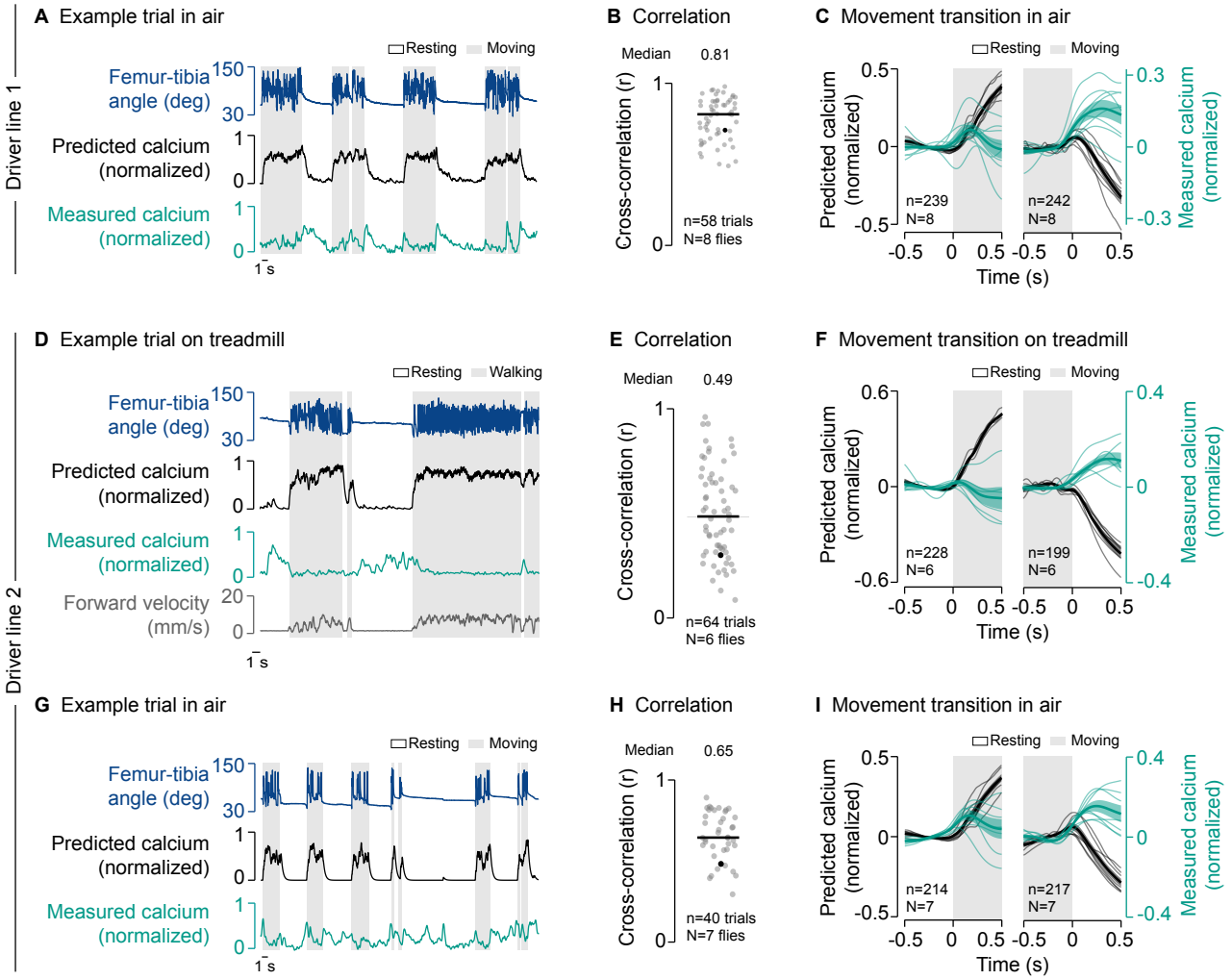

Figure S3.

(A) Example trial of two-photon calcium imaging of hook flexion axons and behavior tracking without the treadmill.

(B) Cross-correlation coefficient between predicted and measured calcium signals per trial at a time lag of zero. The black line shows the median. The black dot marks the trial shown in (A). n: number of trials; N: number of flies.

(C) Predicted and measured calcium signals aligned to the transitions into and out of movement. Signals are baseline subtracted (mean from -0.5 to 0 s). Thin lines show animal means, thick lines show mean of means, shadings show standard error of the mean. n: number of transitions; N: number of flies.

(D) Example trial of two-photon calcium imaging of hook flexion axons (second driver line) and behavior tracking on the treadmill.

(E) Same as (B) but for hook flexion axons (second driver line) imaged on the treadmill.

(F) Same as (C) but for hook flexion axons (second driver line) imaged on the treadmill. Movement includes walking and grooming.

(G) Example trial of two-photon calcium imaging of hook flexion axons (second driver line) and behavior tracking without the treadmill.

(H) Same as (B) but for hook flexion axons (second driver line) imaged without the treadmill.

(I) Same as (C) but for hook flexion axons (second driver line) imaged without the treadmill.

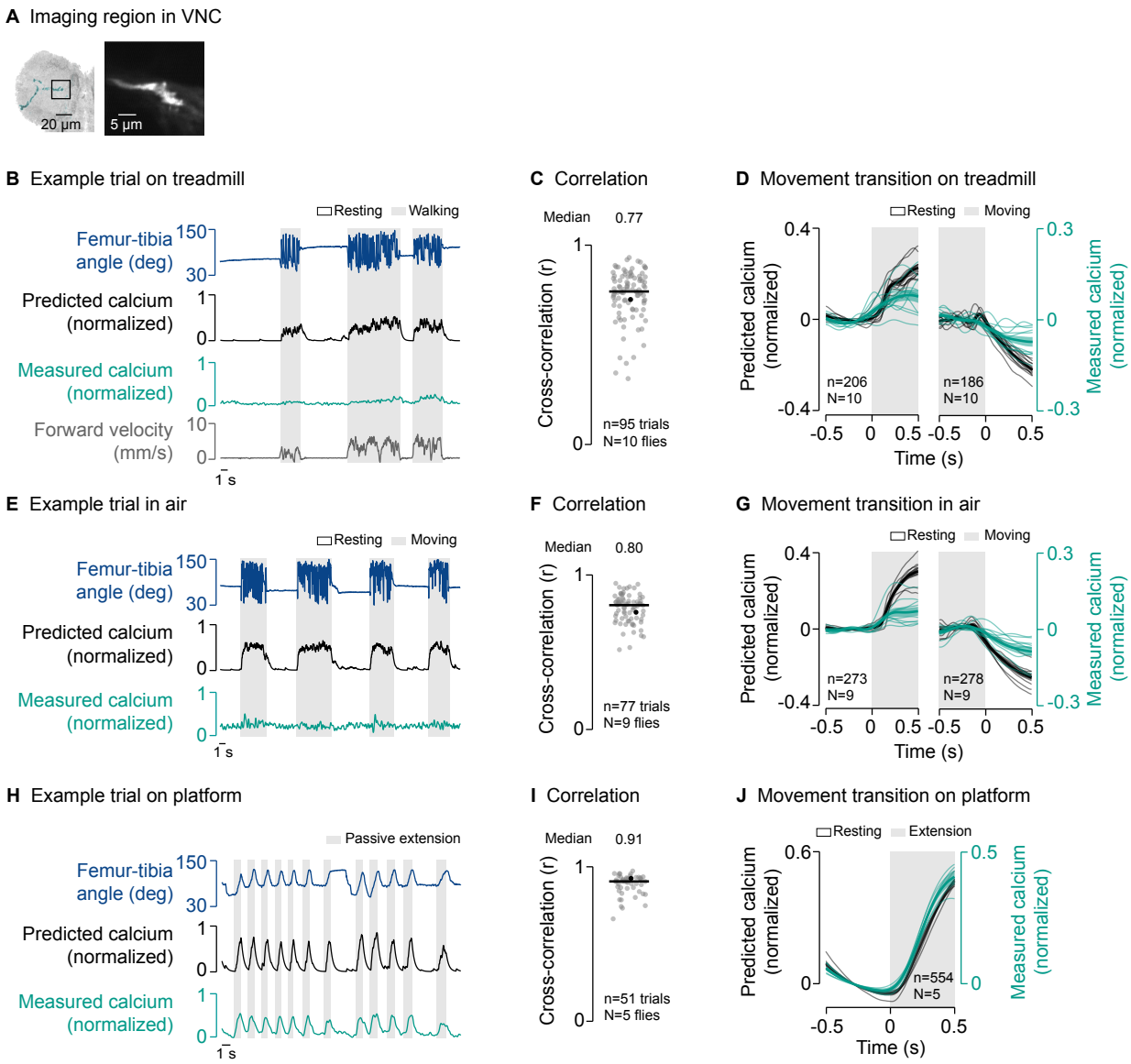

Figure S4.

(A) Left: Confocal image of hook extension axons in the VNC. The black box indicates the imaging region. Green: GFP; gray: neuropil stain (nc82). A: anterior; L: lateral. Right: Mean tdTomato signal within the imaging region during an example trial.

(B) Example trial of two-photon calcium imaging of hook extension axons and behavior tracking on the treadmill.

(C) Cross-correlation coefficient between predicted and measured calcium signals per trial at a time lag of zero. The black line shows the median. The black dot marks the trial shown in (B). n: number of trials; N: number of flies.

(D) Predicted and measured calcium signals aligned to the transitions into and out of movement. Movement includes walking and grooming. Signals are baseline subtracted (mean from -0.5 to 0 s). Thin lines show animal means, thick lines show mean of means, shadings show standard error of the mean. n: number of transitions; N: number of flies.

(E) Example trial of two-photon calcium imaging of hook extension axons and behavior tracking without the treadmill.

(F) Same as (C) but for hook extension axons imaged without the treadmill.

(G) Same as (D) but for hook extension axons imaged without the treadmill.

(H) Example trial of two-photon calcium imaging of hook extension axons and behavior tracking on the platform.

(I) Same as (C) but for hook extension axons imaged on the platform.

(J) Same as (D) but for hook extension axons imaged on the platform.

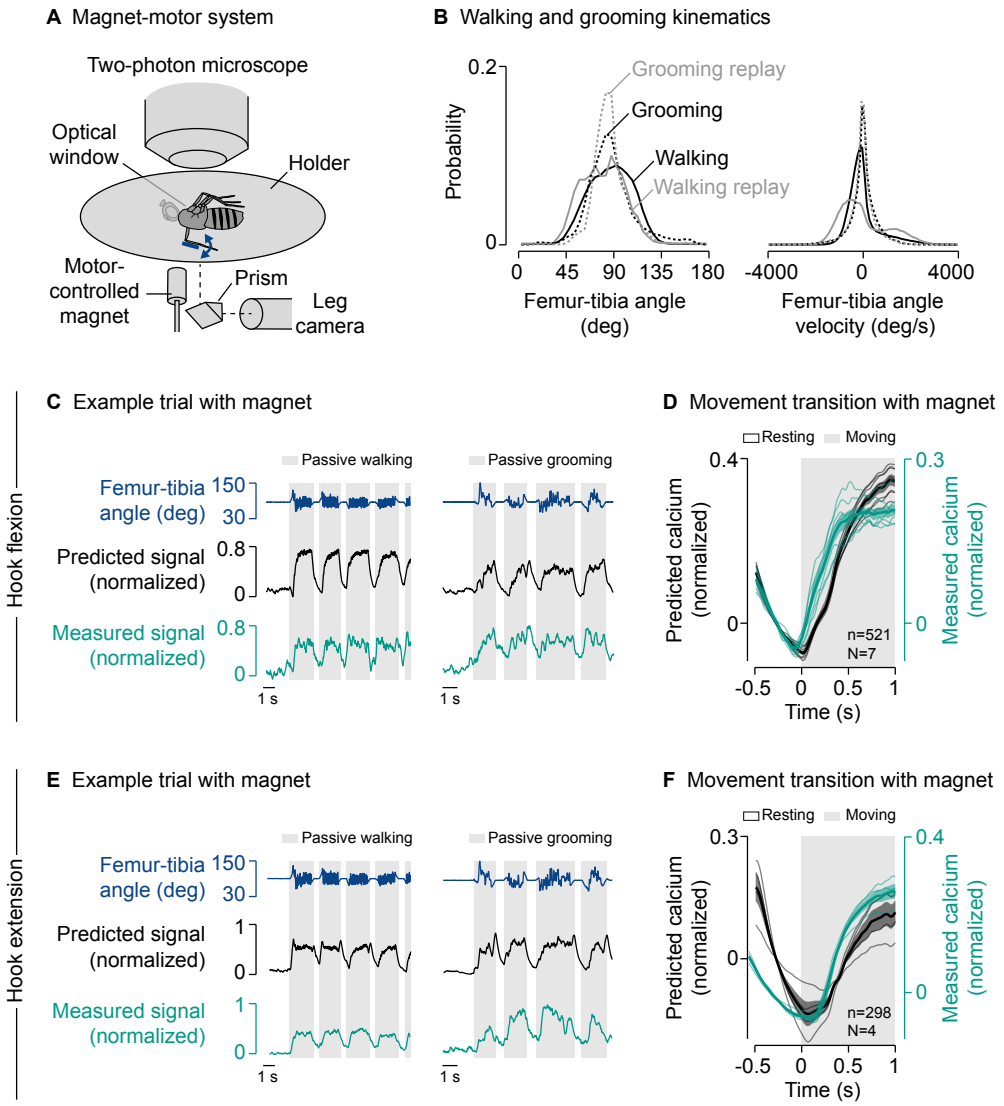

Figure S5.

(A) Experimental setup for two-photon calcium imaging from VNC neurons and leg tracking of a front leg of a tethered fly. All joints except for the femur-tibia joint of a front leg are fixated. The femur-tibia joint is passively moved via a motor-controlled magnet.

(B) Probability distributions of walking and grooming kinematics recorded in the hook flexion neuron dataset and the walking and grooming kinematics used for passive replay with the setup shown in (A).

(C) Example trial of two-photon calcium imaging of hook flexion axons and behavior tracking with the magnet-motor system.

(D) Predicted and measured calcium signals aligned to the transition into passive movement. Movement includes passive walking and passive grooming. Signals are baseline subtracted (mean from -0.5 to 0 s). Thin lines show animal means, thick lines show mean of means, shadings show standard error of the mean. n: number of transitions; N: number of flies.

(E) Same as (C) but for hook extension axons.

(F) Same as (D) but for hook extension axons.

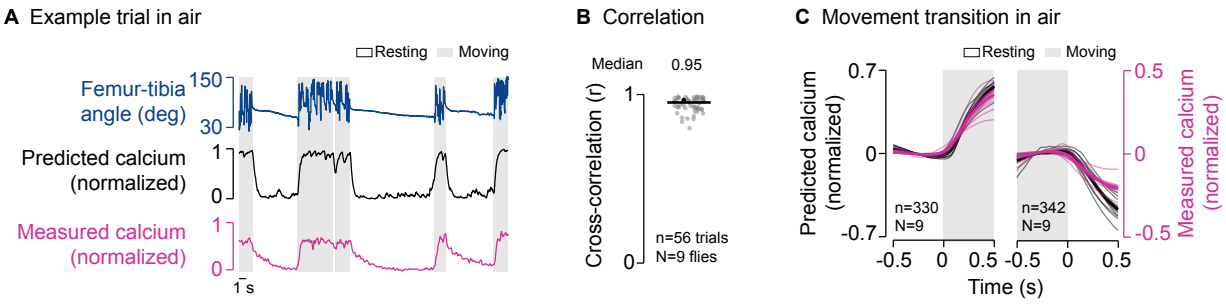

Figure S6.
(A) Example trial of two-photon calcium imaging of 9A neurons and behavior tracking without the treadmill.
(B) Cross-correlation coefficient between predicted and measured calcium signals per trial at a time lag of zero. The black line shows the median. The black dot marks the trial shown in (A). n: number of trials; N: number of flies.
(C) Predicted and measured calcium signals aligned to the transition into and out of movement. Signals are baseline subtracted (mean from -0.5 to 0 s). Thin lines show animal means, thick lines show mean of means, shadings show standard error of the mean. n: number of transitions; N: number of flies.

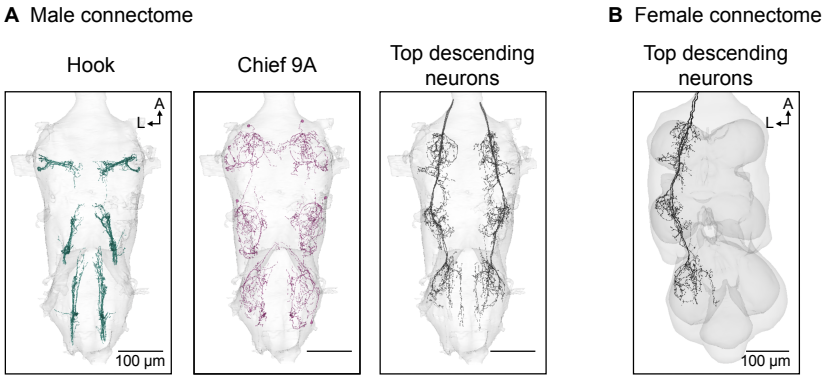

Figure S7.
(A) Hook axons, chief 9A neurons presynaptic to hook axons, and the top two descending neurons presynaptic to the chief 9A neurons in the male VNC connectome (MANC). A: anterior; L: lateral.
(B) Top two descending neurons presynaptic to the chief 9A neuron in the female VNC connectome (FANC). A: anterior; L: lateral.

Supplementary videos

Video S1
Claw axons, hook axons, the chief 9A neuron presynaptic to hook axons, and the top two descending neurons presynaptic to the chief 9A neuron in the FANC connectome.

Video S2
Example trials of two-photon calcium imaging of claw axons and behavior tracking on the treadmill and without the treadmill. Videos are sped up 2x. The measured calcium signal is based on the ratio of GCaMP to tdTomato. For this video, GCaMP images were low-pass filtered using a moving average filter with a time window of 0.2 s. tdTomato images are not shown.

Video S3
Example trials of two-photon calcium imaging of hook flexion axons and behavior tracking on the treadmill, without the treadmill, and on the platform. Videos are sped up 2x. The measured calcium signal is based on the ratio of GCaMP to tdTomato. For this video, GCaMP images were low-pass filtered using a moving average filter with a time window of 0.2 s. tdTomato images are not shown.

Video S4
Example trials of two-photon calcium imaging of 9A axons and behavior tracking on the treadmill, without the treadmill, and on the platform. Videos are sped up 2x. The measured calcium signal is based on the ratio of GCaMP to tdTomato. For this video, GCaMP images were low-pass filtered using a moving average filter with a time window of 0.2 s. tdTomato images are not shown.